The Resolution Dependence of Contiguous U.S. Precipitation Extremes in Response to CO_2 Forcing

KARIN VAN DER WIEL,[a,b] SARAH B. KAPNICK,[b] GABRIEL A. VECCHI,[b] WILLIAM F COOKE,[b,c] THOMAS L. DELWORTH,[b] LIWEI JIA,[a,b] HIROYUKI MURAKAMI,[a,b] SETH UNDERWOOD,[b] AND FANRONG ZENG[b]

[a] *Atmospheric and Oceanic Sciences, Princeton University, Princeton, New Jersey*
[b] *NOAA/Geophysical Fluid Dynamics Laboratory, Princeton, New Jersey*
[c] *University Corporation for Atmospheric Research, Boulder, Colorado*

(Manuscript received 13 April 2016, in final form 27 July 2016)

ABSTRACT

Precipitation extremes have a widespread impact on societies and ecosystems; it is therefore important to understand current and future patterns of extreme precipitation. Here, a set of new global coupled climate models with varying atmospheric resolution has been used to investigate the ability of these models to reproduce observed patterns of precipitation extremes and to investigate changes in these extremes in response to increased atmospheric CO_2 concentrations. The atmospheric resolution was increased from 2° × 2° grid cells (typical resolution in the CMIP5 archive) to 0.25° × 0.25° (tropical cyclone permitting). Analysis has been confined to the contiguous United States (CONUS). It is shown that, for these models, integrating at higher atmospheric resolution improves all aspects of simulated extreme precipitation: spatial patterns, intensities, and seasonal timing. In response to 2 × CO_2 concentrations, all models show a mean intensification of precipitation rates during extreme events of approximately 3%–4% K^{-1}. However, projected regional patterns of changes in extremes are dependent on model resolution. For example, the highest-resolution models show increased precipitation rates during extreme events in the hurricane season in the U.S. Southeast; this increase is not found in the low-resolution model. These results emphasize that, for the study of extreme precipitation there is a minimum model resolution that is needed to capture the weather phenomena generating the extremes. Finally, the observed record and historical model experiments were used to investigate changes in the recent past. In part because of large intrinsic variability, no evidence was found for changes in extreme precipitation attributable to climate change in the available observed record.

1. Introduction

Precipitation is of vital importance to societies and ecosystems around the world (e.g., Jackson et al. 2001). In contrast, extreme precipitation events may have widespread negative impacts. For example, in the contiguous United States (CONUS) these impacts include increased extreme streamflow (Groisman et al. 2001), increased damage from floods (Pielke and Downton 2000), increased outbreaks of waterborne diseases (Curriero et al. 2001), increased soil water stress (Fay et al. 2003; Knapp et al. 2008), and increased crop damage (Rosenzweig et al. 2002). The societal importance of precipitation extremes shows there is a need for reliable projections of how these extreme events may change in response to global climate change.

Theoretical understanding of precipitation extremes is based on the idea that, within an atmospheric column, the precipitation rate P during an extreme event depends on precipitation efficiency ε, vertical velocities $\omega(p)$, and the vertical derivative of saturation specific humidity q_s along a moist adiabat $S(T, p) = dq_s/dp|_{\theta_e^*}$ (O'Gorman and Schneider 2009; O'Gorman 2015):

$$P = -\varepsilon\{\omega(p)S(T,p)\}, \tag{1}$$

where the braces denote the mass-weighted vertical integral. Precipitation efficiency is defined as the total

Denotes Open Access content.

Corresponding author address: Karin van der Wiel, NOAA/Geophysical Fluid Dynamics Laboratory, 201 Forrestal Rd., Princeton, NJ 08540.
E-mail: kwiel@princeton.edu

DOI: 10.1175/JCLI-D-16-0307.1

storage of water vapor in the column and the transport of water vapor to and from the column. In the absence of dynamical or physical changes, the change of extreme precipitation depends on the last factor only—the thermodynamical change of moisture in the atmosphere. This is often simplified to a scaling related to the Clausius–Clapeyron relation of 6%–8% K^{-1}; for each degree of surface warming it is expected that precipitation rates during extreme events increase by 6%–8% (e.g., Allen and Ingram 2002; Trenberth et al. 2003; Pall et al. 2007; Muller et al. 2011; Westra et al. 2014; O'Gorman 2015). However, the relevant location (local, regional, or global) for computing the temperature change is unknown. Therefore, Clausius–Clapeyron scaling can only be used as a first estimate of thermodynamic climate change.

Global climate models can be used to extend such theoretical considerations. Climate sensitivities [change per degree warming (% K^{-1})] estimated from model experiments include thermodynamic, dynamic, and physical contributions to changes in extreme precipitation. Based on analyses of model experiments in phases 3 and 5 of the Coupled Model Intercomparison Project (CMIP3 and CMIP5) archives, which were assessed in the Intergovernmental Panel on Climate Change (IPCC) Fourth Assessment Report (AR4; IPCC 2007) and Fifth Assessment Report (AR5; IPCC 2013), precipitation extreme events are expected to happen more frequently and the extremes are expected to be stronger by the end of the twenty-first century. The sensitivity of extreme precipitation to climate change varies strongly between models and between regions (e.g., Sun et al. 2007; Kharin et al. 2007, 2013; Sillmann et al. 2013; Toreti et al. 2013; Villarini et al. 2013a; Wuebbles et al. 2014; Fischer and Knutti 2015). Furthermore, the sensitivity is larger the more extreme the events that are considered (e.g., the 1-yr vs 5-yr returning events; Shiu et al. 2012; Fischer and Knutti 2015). The conclusions of these modeling studies are complemented by trends in the observed record of extreme precipitation (e.g., Kunkel et al. 1999; Kunkel 2003; Villarini et al. 2013b; Mallakpour and Villarini 2015); however, spatial and temporal availability of station data is often a limiting factor for climate studies.

The societal value of climate projections based on model experiments is limited by, among other factors, the ability of a model to accurately simulate the observed present-day climate. Common model biases related to precipitation include biases in seasonal mean precipitation (dry regions receive too little precipitation and wet regions too much; Sheffield et al. 2013) and an overestimation of the number of days with precipitation (the "drizzle problem"; e.g., Dai 2006; Schubert et al. 2008; Lee et al. 2009; Mehran et al. 2014). The drizzle problem further leads to an overestimation of the frequency of light precipitation and underestimation of the frequency of extreme precipitation. In part, the bias in the distribution of precipitation rates (light vs extreme) reflects a misrepresentation of the atmospheric processes that lead to precipitation in the real world, which are often at scales smaller than those resolved in global climate models (Wehner et al. 2010). Other impacts of coarse model resolution include a smoothing of spatial features such as orography, which limit the reliability of projections on regional scales (Thibeault and Seth 2014; Schoof and Robeson 2016).

Common approaches to work around such issues include the use of high-resolution atmosphere-only models or downscaling techniques. The latter includes methods based on the statistical distribution of precipitation in the present-day climate or further integration with a regional model, to add regional value to coupled model output (e.g., Dibike and Coulibaly 2006; Frei et al. 2006; Gutowski et al. 2010; Ning et al. 2015; Schoof 2015). However, such solutions may not be in dynamical or thermodynamical equilibrium outside the region considered. Furthermore, a regional model's hydrology is often constrained by the large-scale moisture flux convergence prescribed as an outer boundary condition. Global models are needed to represent energetics, dynamics, and moisture consistently. In atmosphere-only models it has been shown that models with higher-resolution grids improve the spatial patterns of seasonal mean precipitation, the statistics of daily precipitation, and the magnitudes of precipitation extremes (Duffy et al. 2003; Iorio et al. 2004; Wehner et al. 2010). However, because of interactions between atmosphere and ocean, coupled atmosphere–ocean models are more suitable tools for studies of climate change than atmosphere-only models.

At the National Oceanic and Atmospheric Administration (NOAA)/Geophysical Fluid Dynamics Laboratory (GFDL) a family of global coupled models has been developed to test the impact of high atmospheric model resolution in a global coupled atmosphere–ocean framework. Three models with identical ocean and sea ice model components have been coupled to atmospheric and land model components of low (2° × 2°; as typically found in the CMIP5 archive), medium (0.5° × 0.5°; a tropical cyclone-permitting model), and high (0.25° × 0.25°) resolution. In this paper, the impact of atmospheric model resolution in a global coupled model framework is investigated for the simulation of extreme precipitation events in the CONUS.

There are two objectives to this study: first, to test the hypothesis that the quality of simulated extreme

precipitation is improved when the horizontal resolution of the atmospheric model component in a fully coupled global climate model is increased and second, to investigate changes in extreme precipitation in response to CO_2 forcing and to investigate whether such projected changes depend on model resolution.

The rest of this paper is organized as follows: The set of coupled models and observation-based data products used in this study are described in section 2. The methodology is discussed in section 3. The results are discussed in section 4. A summary and a final discussion are given in section 5.

2. Models and data

a. Model descriptions

We use a suite of global coupled climate models to evaluate the impact of horizontal atmospheric resolution on the quality of simulated extreme precipitation events and on potential changes in precipitation extremes in the CONUS. The GFDL coupled models—the Low Ocean Atmosphere Resolution (LOAR) model, the Forecast-Oriented Low Ocean Resolution (FLOR) model, and the High-Resolution FLOR (HiFLOR) model—share the same atmosphere, land, ocean, and sea ice model components that were derived for the GFDL Coupled Model version 2.1 (CM2.1; Delworth et al. 2006) and version 2.5 (CM2.5; Delworth et al. 2012). The LOAR model has an horizontal atmospheric resolution of $2° \times 2°$ (C48 grid; i.e., 48×48 grid cells on each face of the cubed sphere). In the FLOR model, the horizontal resolution has been increased to $0.5° \times 0.5°$ (C180 grid). In the HiFLOR model, the horizontal atmospheric grid is further refined to be $0.25° \times 0.25°$ (C384 grid).

In all models, the atmospheric model component is based on a finite-volume dynamical core on a cubed sphere (Putman and Lin 2007), with 32 vertical levels. The dynamical time step is modified to match the individual model's atmospheric resolution. Atmospheric physics is similar to that in GFDL CM2.5 (Delworth et al. 2006, 2012; Vecchi et al. 2014). Convection is parameterized following the relaxed Arakawa–Schubert formulation; large-scale supersaturation is condensed into cloud water from which large-scale precipitation fluxes are derived. Details on these and other parameterization schemes can be found in Anderson et al. (2004). The ocean model component is Modular Ocean Model, version 5 (MOM5; Griffies 2012), configured as in Vecchi et al. (2014), with a $1° \times 1°$ horizontal grid. The land model component is the Land Model, version 3 (LM3; Milly et al. 2014), with an equivalent horizontal resolution as the atmospheric model component. The sea ice model is the Sea Ice Simulator, version 1 (SIS1), as in Delworth et al. (2012). More details on the FLOR model setup can be found in Vecchi et al. (2014) and Jia et al. (2015) and for the HiFLOR model setup in Murakami et al. (2015). To reach radiative balance at the top of atmosphere, cloud parameters were tuned in FLOR. These parameters have not been retuned in LOAR and HiFLOR; therefore, physical parameterizations are the same across models, but LOAR, FLOR, and HiFLOR have a different global mean temperature, with the lowest-resolution model being the warmest and the highest-resolution model being the coldest.

LOAR, FLOR, and HiFLOR have been developed from the older global coupled climate model GFDL CM2.1 (Delworth et al. 2006). The atmospheric dynamical core, the land model component and the ocean model component have been updated. LOAR has a horizontal resolution that is similar to the GFDL CM2.1; however, the vertical atmospheric resolution has been increased from 24 to 32 levels. Since its development, CM2.1 has been used for many climate studies and was part of the IPCC AR4 (IPCC 2007) and AR5 (IPCC 2013). The higher atmospheric and land resolutions of FLOR and HiFLOR have been shown to improve numerous aspects of global climate compared to CM2.1—for example, the seasonal prediction of temperature and precipitation (Jia et al. 2015), sea surface temperatures (SSTs; Stock et al. 2015), sea ice (Msadek et al. 2014), orographic precipitation (Kapnick et al. 2014), and tropical cyclones (Vecchi et al. 2014; Murakami et al. 2015; Zhang et al. 2016). FLOR is considered to be a new base model; LOAR and HiFLOR can be viewed as low- and high-resolution versions of that newly developed base model.

b. Experiment descriptions

Present-day control experiments were created by integrating LOAR, FLOR, and HiFLOR for 300 years with constant 1990 radiative forcing and land-use conditions. These experiments were used to evaluate the quality of the simulated precipitation fields in the three coupled models. Any variability in these experiments is the result of internal variability within the climate system; all external forcing is constant. Years 171–270 were used for analysis in the current paper.

Starting at year 101 of the present-day control experiments, forced integrations with additional CO_2 forcing were performed. For the first 70 years of these experiments, the CO_2 concentration was increased by $1\%\ yr^{-1}$. In year 170 the CO_2 concentration has doubled relative to the present-day control experiment. From year 170 onward, the models were integrated for an additional 100 years with constant, double-CO_2

concentration relative to the present-day control experiments. We will refer to years 171–270 of this integration as the $2 \times CO_2$ experiment.

Finally, an ensemble of historical integrations was created in which the model sea surface temperature SST was restored to the interannually varying observed field SST_T. To do so, a restoring tendency was added to the SST tendency as computed in the coupled model $\mathscr{O}$ over a set restoring time scale τ:

$$\frac{d\mathrm{SST}}{dt} = \mathscr{O} + \frac{1}{\tau}(\mathrm{SST}_T - \mathrm{SST}). \quad (2)$$

The observed SST field was taken from the Met Office Hadley Centre Sea Ice and SST dataset (HadISST1.1; Rayner et al. 2003). The historical experiment consists of six ensemble members each for FLOR and HiFLOR and covers the period 1971–2012 (three with $\tau = 5$ days and three with $\tau = 10$ days). Individual ensemble members have been created using different initial conditions generated from a previous set of restoring experiments; more details can be found in Murakami et al. (2015).

In all experiments the models were integrated globally but analysis in this paper is restricted to the CONUS.

c. *Observationally based data*

The simulated precipitation data are compared to the National Centers for Environmental Prediction (NCEP)/Climate Prediction Center (CPC) unified gauge-based analysis of daily precipitation over the CONUS (Higgins et al. 2000). This dataset provides estimates of daily precipitation totals on a $0.25° \times 0.25°$ grid for the CONUS. The estimates are based on gauge data, interpolated using the optimal interpolation scheme of Gandin and Hardin (1965) (Chen et al. 2008). The CPC dataset covers the time period 1 January 1948–31 December 2006. To address uncertainties in the CPC data and their potential impact on the result of this study, similar analyses as those presented have been performed on other datasets based on different observational data sources. The results of these analyses are documented in the appendix and will be referenced throughout this study.

3. Methods

There are many different definitions of extreme events in the scientific literature. For precipitation, these are generally based on either precipitation rates (e.g., total annual precipitation, annual maximum daily or monthly precipitation, and the precipitation rate of the 99th percentile of daily or monthly precipitation; Sen Roy and Balling 2004; Min et al. 2011; O'Gorman 2015) or the number or duration of precipitation events (e.g., number of days with precipitation exceeding 25 mm, frequency of wet days, and the duration of dry periods; Curriero et al. 2001; Durman et al. 2001; Sen Roy and Balling 2004). In some cases the resulting data are fitted to a statistical distribution (e.g., a generalized extreme value distribution or z scores; Curriero et al. 2001; Min et al. 2011).

Here, we have chosen to focus on the precipitation rate (i.e., intensity) of daily precipitation events with a 1- and 5-yr return period. All days of the year were included in the analysis—both days with precipitation and days without precipitation. We did not fit a statistical distribution to the data before analysis because the model integrations were sufficiently long to accurately estimate the precipitation rate of the 1- and 5-yr returning event. In addition to annual extremes, we have also investigated seasonal extreme events, using events with a 1- or 5-season return period. For the evaluation of the quality of simulated precipitation in the different models (section 4a), we have also computed the simple daily intensity index (SDII; e.g., Peterson et al. 2008), which is a measure of the mean precipitation rate on days with precipitation. The SDII is computed by dividing the total annual precipitation by the number of days with precipitation equal or greater than 1 mm.

Potential changes in extreme precipitation due to climate change were investigated using the $2 \times CO_2$ experiments. We investigated the change in the precipitation rate of the 1- or 5-yr returning events, as well as the change of the seasonality of extreme events.

To identify trends of extreme precipitation, we used the peak-over-threshold approach; that is, for every year we counted the number of days with precipitation exceeding the precipitation rate of the 1- or 5-yr returning event. By design, the mean of these counts is 1.0 and $0.2\,\mathrm{yr}^{-1}$, respectively. We have used a Poisson regression model to examine whether trends exist in the frequency of extreme precipitation events, as was done in Villarini et al. (2013b) and Mallakpour and Villarini (2015). Poisson regression was chosen because the data are discrete (yearly counts), and it is assumed that the data follow a Poisson distribution. We fitted a Poisson model that depended linearly on time through a logarithmic link function:

$$\lambda_i = \exp(\beta_0 + \beta_1 t_i), \quad (3)$$

in which λ_i is the predicted number of extreme events for year t_i. If coefficient β_1 was different from zero at a 5% significance level, we have reported that grid point as having a trend in the frequency of extreme events.

For the CPC data, to reduce the influence of noise, we have taken into account a box of 3×3 grid points

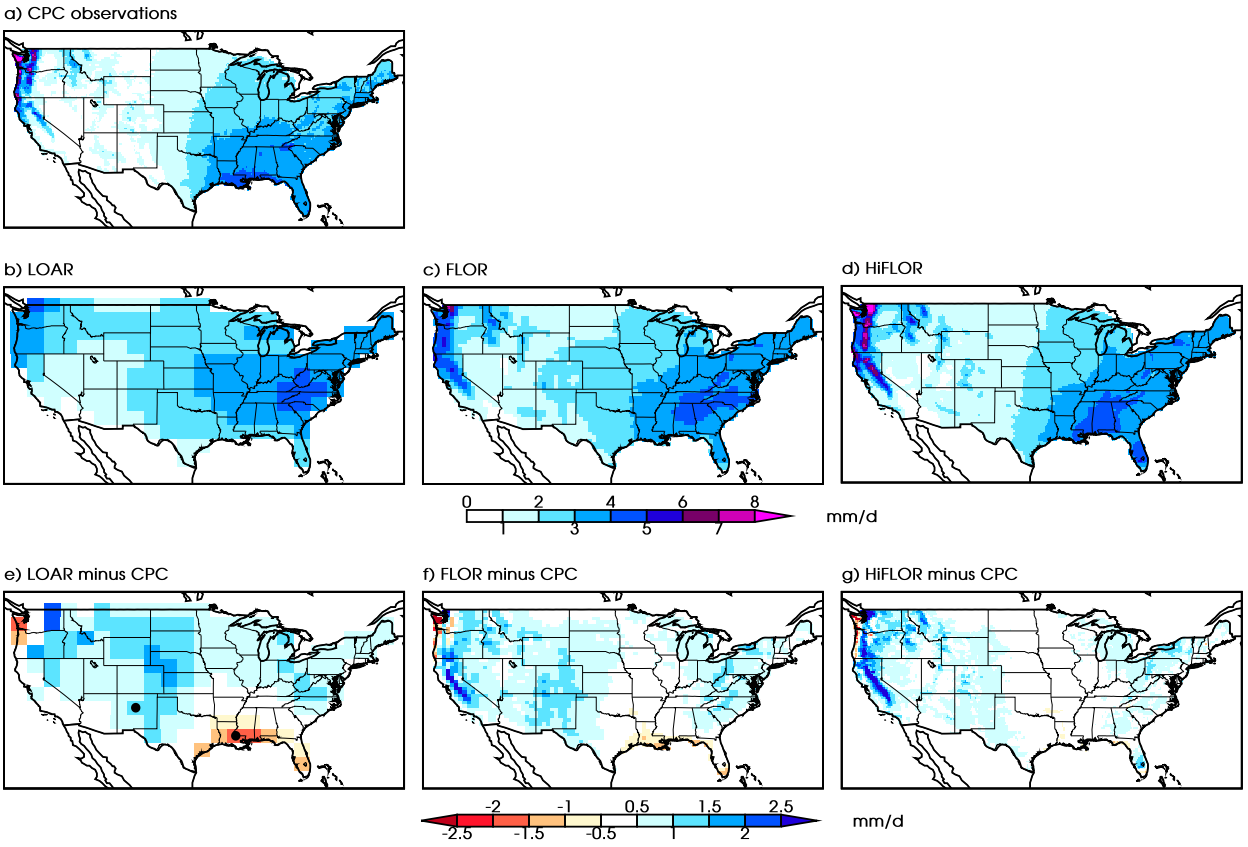

FIG. 1. Annual mean precipitation rate (mm day^{-1}) in (a) CPC observations, (b) LOAR, (c) FLOR, and (d) HiFLOR. Difference between the model simulations and the observations (mm day^{-1}) for (e) LOAR, (f) FLOR, and (g) HiFLOR. Black dots in (e) indicate the locations of Santa Fe, New Mexico, and New Orleans, Louisiana (see text).

around each grid point when counting the extreme events. This corrects for storm systems that are shifted by one grid point (~25 km) in any direction but do exceed the threshold. The computed trends using this 3×3 box method are of similar size as the computed trends using the normal one-gridpoint method; however, a much larger fraction of the grid points showed a statistically significant trend when the 3×3 box method was used. For the model data this correction was not necessary because of the availability of the ensemble of historical integrations.

Chen and Knutson (2008) discuss the influence of different interpretations of simulated precipitation data on the evaluation of extreme precipitation in climate models. Following their recommendation, we interpret model-simulated precipitation data as area mean estimates rather than point-based estimates. Therefore, in section 4a all output from FLOR and HiFLOR and the CPC data have been remapped onto the LOAR horizontal grid to facilitate a fair comparison of the three models and the observed data. When output from FLOR and HiFLOR is compared, the analysis has been done on the FLOR horizontal grid. All remapping was done by means of a conservative remapping scheme and was done before the computation of any index of (extreme) precipitation.

4. Results

a. *Evaluation of simulated precipitation in coupled models with increasing horizontal atmospheric model resolution*

As shown in the spatial distribution of the annual mean precipitation rate in the CPC observations (Fig. 1a) and in the present-day control experiment of the three models (Figs. 1b–d), FLOR and HiFLOR both improve the simulated pattern compared to LOAR. The observed east–west precipitation gradient is most realistic in HiFLOR, although it is not as strong as observed. The western CONUS is too wet in all models (Figs. 1e–g). The precipitation maximum along the Gulf Coast is most realistic in HiFLOR; the dry bias decreases with increasing *horizontal* atmospheric resolution. The spatial pattern of precipitation biases is similar

TABLE 1. CONUS mean statistics of annual mean precipitation rate (mm day^{-1}); included are the spatial mean, mean bias, RMSE, and pattern correlation (corr). Boldface values are shown for the best-performing model by that measure. Note that the data have been remapped onto relevant lower resolution horizontal grids before computation of the mean and statistics.

Model or dataset	Grid	Mean	Bias	RMSE	Corr
CPC	LOAR	2.07	—	—	—
LOAR	LOAR	2.67	0.60	0.90	0.78
FLOR	LOAR	2.64	0.57	0.73	0.92
HiFLOR	LOAR	2.55	**0.48**	**0.61**	**0.93**
CPC	FLOR	2.07	—	—	—
FLOR	FLOR	2.65	0.57	0.79	0.88
HiFLOR	FLOR	2.54	**0.47**	**0.67**	**0.91**
CPC	HiFLOR	2.07	—	—	—
HiFLOR	HiFLOR	2.54	0.47	0.69	0.90

in all models, except Florida, which is too dry in LOAR and too wet in HiFLOR. The size of the biases decreases with increasing horizontal atmospheric resolution.

Furthermore, the increased horizontal spatial resolution in FLOR and HiFLOR allows for a more realistic representation of orography (Delworth et al. 2012; Kapnick and Delworth 2013). Consequently, the precipitation maximum associated with the Sierra Nevada and Cascade Range appears in FLOR and HiFLOR, although precipitation is overestimated compared to CPC data. This wet bias is not present in LOAR, which makes direct model comparison for this region difficult: LOAR seems to get ''better'' values, although it is for the wrong reason—the absence of realistic orography. As a side note, there is evidence that conventional gridded precipitation products, including the CPC dataset used here, severely underestimate precipitation over the western CONUS mountain ranges (Lundquist et al. 2015). The wet bias of FLOR and HiFLOR to reality may, therefore, not be as grave over the Sierra Nevada and Cascade Range as one would infer from this comparison.

For a more quantitative comparison, all high-resolution data are first remapped to a common low-resolution grid (Chen and Knutson 2008). As discussed in section 3, such a procedure ensures that an equal comparison of area mean precipitation rates with equal degrees of freedom (grid points) is made. On a common $2° \times 2°$ grid (as in LOAR) over the CONUS, the highest-resolution model (HiFLOR) performs best (Table 1, top four rows). The CONUS mean precipitation bias decreases, the root-mean-square error (RMSE) decreases, and the pattern correlation increases with increasing horizontal atmospheric resolution. The comparison on a common $0.5° \times 0.5°$ grid (as in FLOR) shows HiFLOR improves the simulation of mean precipitation from FLOR (Table 1, rows 5–7).

As discussed before, besides correct simulation of mean precipitation the simulation of extreme precipitation is highly relevant for society. The spatial distribution of the precipitation rate for the 1-yr returning event in CPC observations and associated model biases are shown in Fig. 2. For completeness and to show the impact of remapping, the observed distribution and model biases are shown on all model grids.

The largest precipitation intensities of the 1-yr returning event in the observed data are found along the Gulf Coast (70–110 mm day^{-1}) and the Pacific coast, Sierra Nevada, and Cascade Range (70–150 mm day^{-1}; Fig. 2c). Furthermore, the Appalachian Mountains are a local maximum. Generally, the precipitation rate during extreme events decreases traveling inland and is higher in regions with higher mean precipitation. The pattern correlation of annual mean precipitation (Fig. 1a) and the precipitation rate of the 1-yr returning event (Fig. 2c) is 0.89. If the CPC data are remapped to lower-resolution horizontal grids these patterns are generally maintained, although the precipitation rate decreases (e.g., the precipitation rate along the Gulf Coast is 70–90 mm day^{-1} on the FLOR grid and 50–70 mm day^{-1} on the LOAR grid; Figs. 2a,b). However, the extrema on the West Coast, on the windward sides of the mountain ranges, are not evident once the data are coarsened.

As was found for the annual mean precipitation rate, model biases of the 1-yr returning event have a similar pattern in all models and decrease with increasing horizontal atmospheric resolution (Figs. 2d–i). Areas with a mean dry bias are areas in which the precipitation rate during the 1-yr returning event is underestimated (e.g., the Gulf Coast); areas with a mean wet bias are areas in which precipitation associated with the 1-yr returning event is overestimated (e.g., the U.S. Southwest). The Sierra Nevada are a hot spot for model bias in FLOR and HiFLOR, although the comparison is based on an observational data product that underestimates mean and extreme precipitation there (Lundquist et al. 2015).

Quantitatively, on the LOAR grid, HiFLOR outperforms the other two models (i.e., lower mean bias, lower RMSE, and higher pattern correlation; Table 2, top four rows). On the FLOR grid, HiFLOR is less biased than FLOR (Table 2, rows 5–7). There is a consistent improvement of the simulated 1-yr returning event of precipitation when the atmospheric model resolution is increased in a global coupled model for the yearly returning event (Fig. 2 and Table 2) and events in individual seasons (not shown).

A similar analysis was done for the precipitation rate of the extreme event with a 5-yr return period. The spatial pattern of precipitation rate was found to be very similar to that of the 1-yr returning event (pattern

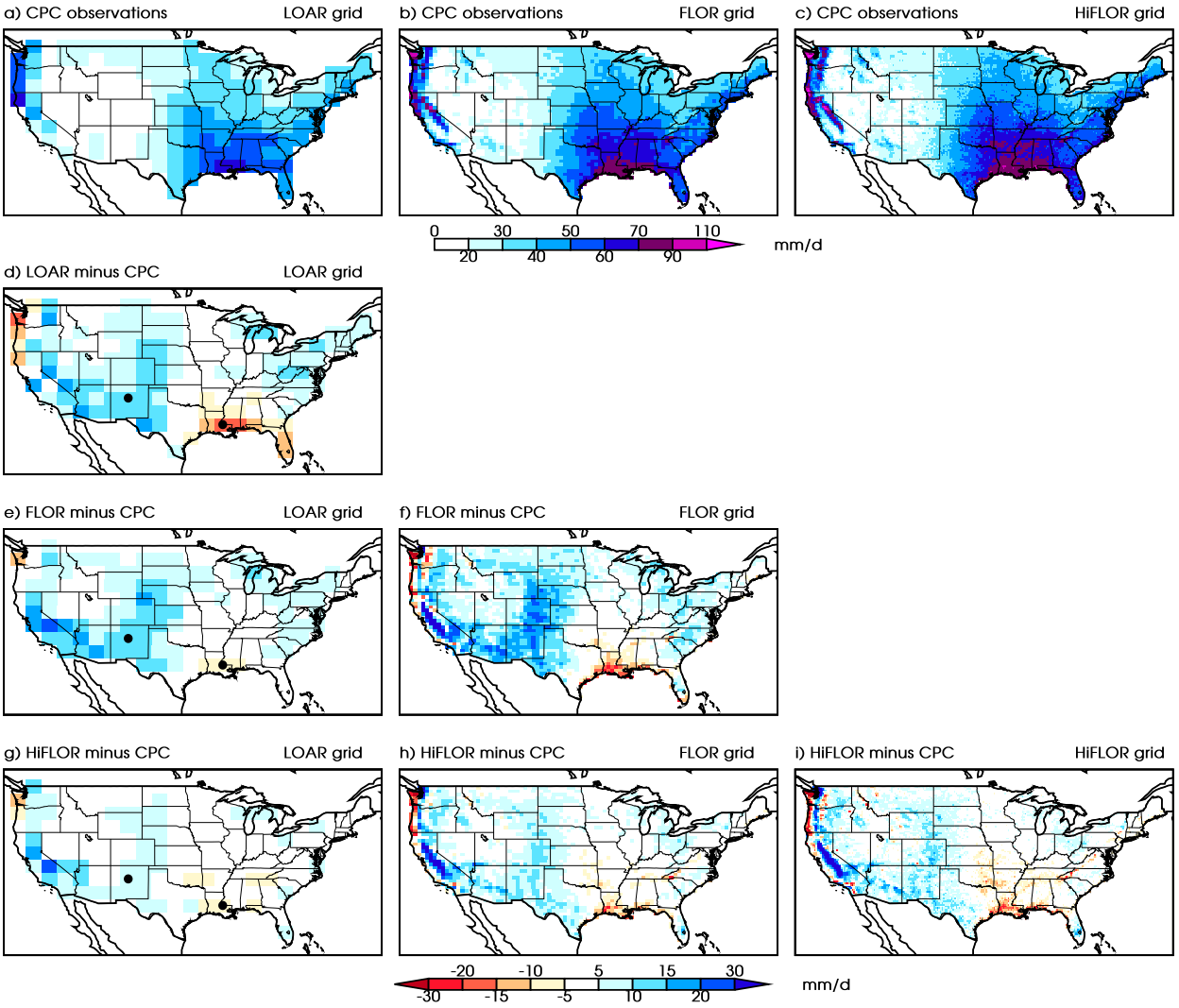

FIG. 2. (a)–(c) The 1-yr returning event of daily precipitation rate (mm day^{-1}) in CPC observations on different horizontal grids. Differences between model simulations and the CPC observations (mm day^{-1}) for (d) LOAR, (e),(f) FLOR, and (g)–(i) HiFLOR using different horizontal grids. Shown are data on the (a),(d),(e),(g) LOAR grid, (b),(f),(h) FLOR grid, and (c),(i) HiFLOR grid. Black dots in (d),(e),(g) denote the locations as in Fig. 1e.

correlation of 0.98 for CPC data; figure not shown for the 5-yr returning event). The 5-yr precipitation intensities are 100–200 mm day^{-1} along the Pacific coast and 120–160 mm day^{-1} for the Gulf Coast region. For the 5-yr returning event there is also a consistent decrease of the mean bias and the RMSE and an increase in the pattern correlation from LOAR to FLOR to HiFLOR (Table 2), the higher-resolution models simulate a more realistic precipitation distribution.

In the appendix a similar verification of model simulated extreme precipitation rates is presented based on different observational data products. The results from that analysis are in agreement with the results presented above; increased horizontal atmospheric resolution improves the ability of the model to capture extreme precipitation patterns.

Although not a measure of extreme precipitation, the SDII gives an indication of whether models have a drizzle problem—that is, an overestimation of the number of days with precipitation and/or an underestimation of the mean precipitation rate on a wet day (minimum 1 mm day^{-1} precipitation). From Table 2 it is obvious the models do not have a drizzle problem over the CONUS; the SDII is generally too high in the models. However, the RMSE decreases and pattern correlation increases with increasing atmospheric resolution, resulting in FLOR and HiFLOR being less biased than LOAR and HiFLOR being less biased than FLOR.

TABLE 2. As in Table 1, but for the annual 1-yr returning event, the annual 5-yr returning event, and the SDII of precipitation (mm day^{-1}).

		1-yearly event				5-yearly event				SDII			
Model or dataset	Grid	Mean	Bias	RMSE	Corr	Mean	Bias	RMSE	Corr	Mean	Bias	RMSE	Corr
CPC	LOAR	31.23	—	—	—	44.46	—	—	—	6.29	—	—	—
LOAR	LOAR	35.60	4.37	8.51	0.85	49.03	4.57	12.94	0.80	6.69	**0.40**	1.01	0.86
FLOR	LOAR	36.69	5.46	7.65	0.92	49.53	5.07	10.12	0.91	6.88	0.59	0.95	0.91
HiFLOR	LOAR	34.05	**2.82**	**5.34**	**0.94**	46.16	**1.70**	**7.86**	**0.93**	6.69	**0.40**	**0.71**	**0.94**
CPC	FLOR	39.04	—	—	—	57.83	—	—	—	7.53	—	—	—
FLOR	FLOR	45.02	5.98	10.64	0.86	63.44	5.62	15.53	0.83	7.74	**0.21**	1.25	0.85
HiFLOR	FLOR	42.59	**3.56**	**7.88**	**0.91**	60.34	**2.52**	**11.95**	**0.89**	7.78	0.25	**1.04**	**0.90**
CPC	HiFLOR	41.70	—	—	—	62.50	—	—	—	8.08	—	—	—
HiFLOR	HiFLOR	44.21	2.51	8.47	0.90	63.03	0.53	13.50	0.87	8.00	−0.08	1.22	0.88

To examine the distribution of precipitation rates in more detail, histograms of precipitation rates for each model are shown in Figs. 3a–c. More quantitative comparisons are provided by computing the precipitation frequencies in different categories (Figs. 3d–f) and the contribution of each category to the annual total precipitation (Figs. 3g–i). Precipitation categories were chosen to match an equivalent analysis in Dai (2006).

For the CONUS as a whole, there is not much difference between the three models. The distribution of precipitation in the models is very close to the observed distribution of precipitation rates, although LOAR underestimates the frequencies of the most intense precipitation rates (Fig. 3a). The vertical lines for the annual 1-yr returning event show the mean value and model bias as also noted in Table 2. Again, there is no clear indication of a drizzle problem in the models; the frequency of light precipitation ($<$10 mm day^{-1}; Fig. 3d) and the contribution of light precipitation to the total annual precipitation (Fig. 3g) are underestimated. The models slightly overestimate the contribution to total precipitation and frequency of heavy precipitation ($>$10 mm day^{-1}).

However, local biases are larger than the CONUS mean bias (cf. values in Tables 1 and 2 with values in Figs. 1 and 2, respectively). Therefore figures for two specific locations have been added: for the grid point closest to New Orleans, Louisiana (Figs. 3b,e,h), and for the grid point closest to Santa Fe, New Mexico (Figs. 3c,f,i). These points were chosen such that there was one located in a region with a wet bias and one in a region with a dry bias (see black dots in Figs. 1e and 2d,e,g). For these local points there are clear differences between the models. In New Orleans, a location with high mean precipitation and large precipitation extremes, LOAR underestimates the high tail of the distribution of precipitation rates (Fig. 3b). This underestimation bias is decreased in FLOR and HiFLOR. For precipitation rates above 50 mm day^{-1} HiFLOR is the best of these models; note that the observed local 1-yr returning event is 61 mm day^{-1} (CPC observations remapped to LOAR horizontal grid). In Santa Fe, a location of low mean precipitation and weak extremes, all models overestimate the high tail of precipitation rates (Fig. 3c). HiFLOR is the only one of these models that has a distinctive peak in the 1–5 mm day^{-1} category for the contribution to the total precipitation, which is so clear in observations (Fig. 3i). LOAR has a too-flat distribution of precipitation amounts over the middle categories, where the observations show a sharp decline. The overestimation of precipitation rates in the high tail is reduced in HiFLOR, although still remains.

The above results of improved spatial patterns of mean and extreme precipitation, CONUS mean statistics and precipitation distribution are all for the annual mean, taking into account all days in the year. We have repeated these analyses for individual 3-month seasons (not shown) and find that the results are robust; increasing horizontal atmospheric model resolution systematically improves the simulation of precipitation in the CONUS, and HiFLOR provides the best simulation results of these models.

b. *Changes in extreme precipitation in a double-CO_2 climate*

In the models, doubling the CO_2 concentration leads to changes of the CONUS mean annual mean daily precipitation. Relative to the value in the present-day control experiment (CTRL), the change is 1.5% in LOAR, 0.2% in FLOR, and −0.2% in HiFLOR (Table 3). The global mean change of annual mean precipitation is larger: 2.4%, 3.0%, and 3.0% for LOAR, FLOR, and HiFLOR, respectively. The small CONUS mean value of change is the mean of larger increases (wetter conditions in 2 × CO_2) in the northern CONUS and decreases (drier conditions in 2 × CO_2) in the southern CONUS in all models (Figs. 4a–c). Local changes are substantial; for example, in Texas the

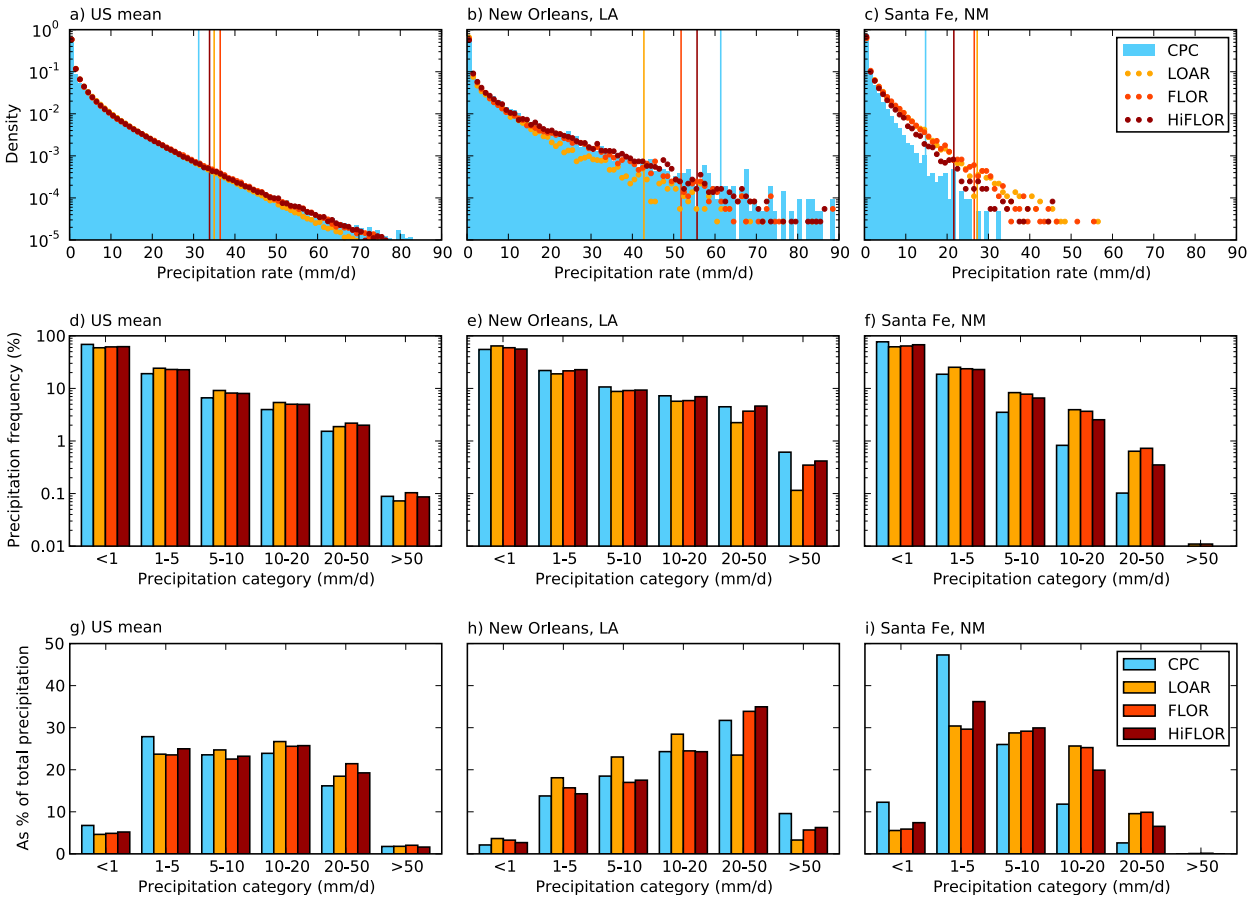

FIG. 3. (a)–(c) Histograms of precipitation distribution in CPC observations (bars), with model histogram data overlaid (scattered dots). Vertical lines denote the precipitation rate of the 1-yr returning event. (d)–(f) Frequency of precipitation rates within set categories (%). (g)–(i) Contribution of precipitation within categories to the annual total precipitation (%). Shown are mean values for (a),(d),(g) CONUS, (b),(e),(h) New Orleans, and (c),(f),(i) Santa Fe. All data were remapped to the LOAR grid before analysis.

decrease exceeds 20% in FLOR. Local changes are smaller in HiFLOR. The patterns of change in DJF and JJA are similar to what was found in the CMIP5 archive (Maloney et al. 2014).

The changes are larger for individual seasons. The largest positive change is in December–February (DJF; Table 3), in which most of the CONUS shows precipitation increases (Figs. 4d–f). In March–May (MAM) the north–south division is very prominent (Figs. 4g–i). As was the case for the annual mean, the local changes are smaller in HiFLOR. In June–August (JJA) mean precipitation decreases in most of the CONUS (Figs. 4j–l). Local decreases exceed 40% in LOAR and FLOR; however, those are found in regions in which summer precipitation is weak. Changes in September–November (SON) are weaker than in other seasons (Figs. 4m–o).

The CONUS mean precipitation rate of the annual 1-yr returning event increases by 11% relative to the 1-yr event in the present-day control experiment in LOAR. In FLOR and HiFLOR the increase is slightly weaker but still substantial: 8.6% and 7.3%, respectively (Table 3). The CONUS mean change of the annual 5-yr returning event is larger: 12%, 9.7%, and 8.8% for LOAR, FLOR, and HiFLOR, respectively. This is in agreement with other studies that found that the more extreme the event considered, the larger the change in response to global warming (Shiu et al. 2012; Fischer and Knutti 2015).

Thermodynamic-forced changes of extreme precipitation depend on mean heating of the lower troposphere (O'Gorman 2015). As discussed in G. A. Vecchi et al. (2016, manuscript in preparation), LOAR is the warmest of these models, and HiFLOR is the coolest model. These differences are the result of a small radiative imbalance in LOAR and HiFLOR (see section 2a). CONUS mean surface warming in response to 2 × CO_2 varies between 2.5 and 2.7 K in the annual mean (Table 3) and is stronger than global mean surface warming. The model differences in temperature change are in part due to differences in oceanic heat uptake between the different models (G. A. Vecchi et al. 2016, manuscript in preparation). However,

TABLE 3. CONUS mean change of surface temperature ΔT (K) and mean precipitation ΔP, ΔP intensity of the 1-yr returning event, and ΔP intensity of the 5-yr returning event (given in mm day^{-1}, % of CTRL value, and % K^{-1} local surface warming) in the 2 × CO_2 experiments. Values for the 1- and 5-season returning events are also shown.

			ΔP mean			ΔP 1-yearly event			ΔP 5-yearly event		
Model	Period	ΔT (K)	mm day^{-1}	%	% K^{-1}	mm day^{-1}	%	% K^{-1}	mm day^{-1}	%	% K^{-1}
LOAR	Annual	2.67	0.07	1.54	0.75	3.86	10.79	4.11	5.87	12.20	4.61
FLOR	Annual	2.69	0.03	0.23	0.16	3.96	8.56	3.25	6.12	9.69	3.65
HiFLOR	Annual	2.53	0.02	−0.16	0.02	3.31	7.31	3.06	5.53	8.82	3.71
LOAR	DJF	2.32	0.24	11.19	4.69	3.11	14.15	6.07	5.43	17.38	7.42
FLOR	DJF	2.41	0.13	6.02	2.63	2.54	10.41	4.71	4.59	12.78	5.71
HiFLOR	DJF	2.32	0.08	3.24	1.35	1.67	7.11	3.20	3.05	9.01	3.99
LOAR	MAM	2.26	0.14	1.84	1.33	2.22	7.33	3.65	3.93	9.88	4.83
FLOR	MAM	2.67	0.12	4.24	2.22	2.44	8.80	3.77	4.24	10.11	4.20
HiFLOR	MAM	2.45	0.09	2.86	1.42	1.94	6.79	3.04	3.41	7.88	3.48
LOAR	JJA	3.28	−0.16	−11.67	−3.17	−0.16	−3.74	−1.12	0.39	−0.68	−0.09
FLOR	JJA	3.02	−0.10	−6.10	−2.18	1.36	2.29	0.56	3.75	6.54	2.01
HiFLOR	JJA	2.88	−0.09	−4.18	−1.31	1.29	3.56	1.36	3.66	7.83	2.98
LOAR	SON	2.81	0.04	1.38	0.58	2.01	8.58	3.20	4.23	11.52	4.19
FLOR	SON	2.65	−0.04	−2.91	−0.86	1.84	5.83	2.41	4.35	9.31	3.62
HiFLOR	SON	2.49	−0.02	−1.16	−0.27	1.98	6.63	2.89	4.32	9.17	3.95

a part of the model differences is from different patterns in warming; CONUS warming does not scale consistently to global mean warming in the models—the CONUS warming is 119%, 123%, and 139% of global warming, in LOAR, FLOR, and HiFLOR, respectively.

For the computation of the climate sensitivity of CONUS extreme precipitation, the mean increase of extreme precipitation per degree warming, an ambiguous decision on which temperature change to consider needs to be made. For example, is it local surface temperature change, local tropospheric air temperature change, regional temperature change, or global temperature change that controls changes in precipitation? As a first-order approximation, we take into consideration the local surface temperature change when climate sensitivities are computed (i.e., the temperature change for each grid point separately). The annual 1-yr returning event increases by 3.1%–4.1% K^{-1} in the models, and the annual 5-yr returning event increases by 3.7%–4.6% K^{-1} (Table 3). The precipitation rate associated with the 5-yr returning event increases more than that associated with the 1-yr returning event. All models, for both extreme event intensities, are below the theoretical thermodynamical approximation of 6%–8% K^{-1} estimated from Clausius–Clapeyron scaling. FLOR and HiFLOR show a lower sensitivity of the extreme events to warming. As a result of the increased horizontal resolution and associated smaller dynamical time step, higher-resolution models tend to have a larger percentage of their precipitation coming from the large-scale parameterization of precipitation rather than from the convective parameterization of precipitation than do lower-resolution models. This is likely caused by the increased number of dynamical time steps per physics time step. The difference in parameterization of simulated precipitation might be one reason for the model differences.

Besides different mean thermodynamic responses, there are differences in the spatial pattern of change of the annual 1-yr returning precipitation event between LOAR, FLOR, and HiFLOR (Figs. 5a–c). In LOAR the largest changes are found in the U.S. Northeast, with very little sensitivity in the Southwest. In HiFLOR the largest increases are found in the eastern CONUS: near the Great Lakes and in the Southeast. A highly sensitive location for increasing extreme precipitation is found along the Atlantic coast from North Carolina to Florida. The pattern from FLOR is somewhere between LOAR and HiFLOR, with the largest changes in the north and east. The differences in sensitivity between the models are investigated in more detail by exploring changes in individual seasons.

In DJF (Figs. 5d–f) the LOAR pattern of change is similar to the annual pattern of change; the extremes in the Northeast increase in size in response to CO_2-induced climate change, and in the southern CONUS the changes are smaller. The Great Plains show increases that are larger than in the annual mean. Furthermore, the Gulf Coast is a location of increasing extreme precipitation in FLOR. The amplitude of change is smaller in HiFLOR than in FLOR and LOAR. In part, this can be explained by the thermodynamical argument: FLOR warms slightly more than HiFLOR in DJF (Table 3). Along the Mexican border there is a

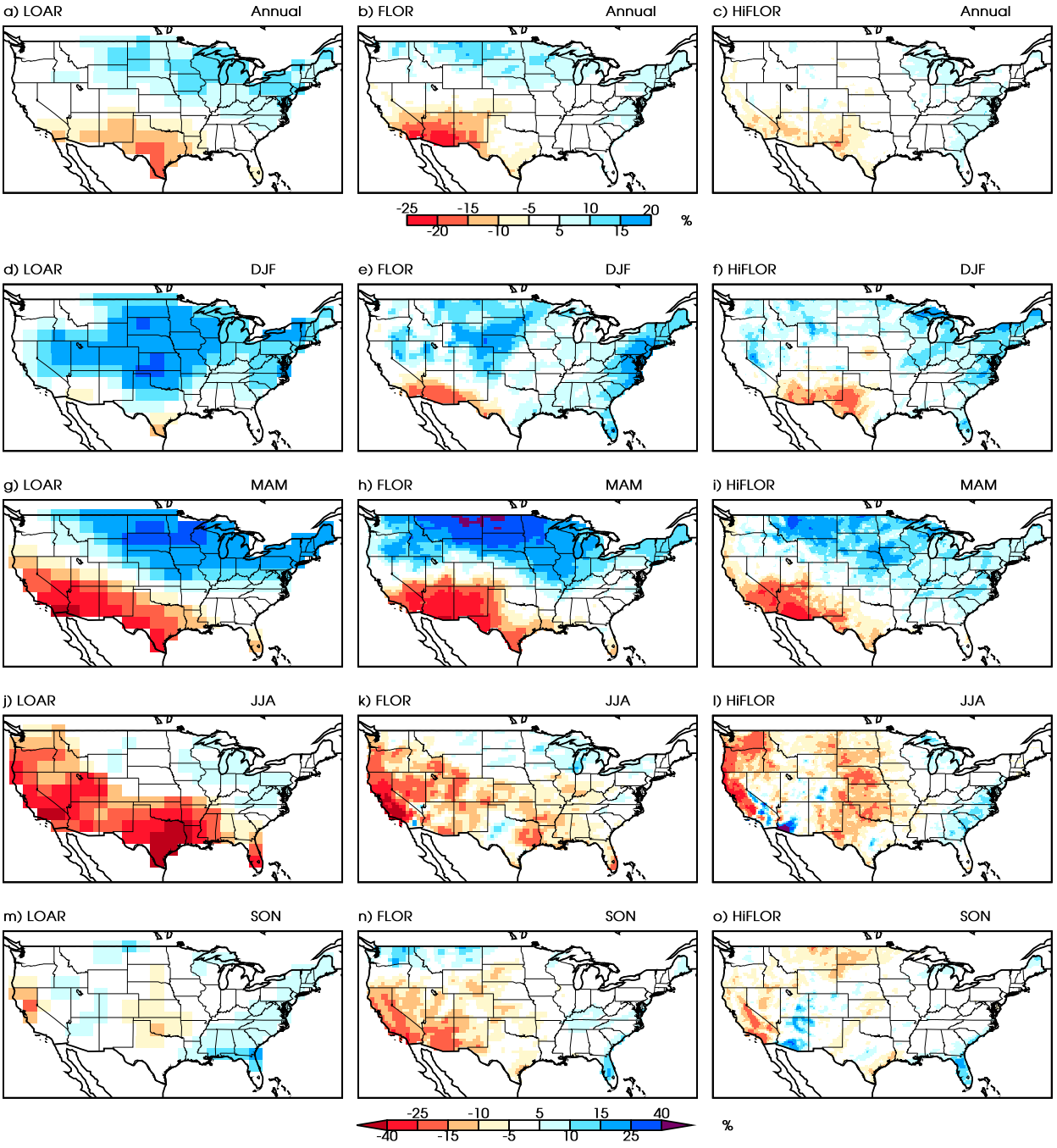

FIG. 4. Relative increase of the mean daily precipitation in the $2 \times CO_2$ experiments {[$(2 \times CO_2) - CTRL$]/CTRL; %} for (a),(d),(g),(j),(m) LOAR, (b),(e),(h),(k),(n) FLOR, and (c),(f),(i),(l),(o) HiFLOR models. Time periods shown are (a)–(c) annual, (d)–(f) DJF, (g)–(i) MAM, (j)–(l) JJA, and (m)–(o) SON.

decrease of mean precipitation (Figs. 4d–f); the 1-yr returning event decreases also, although the decrease is weaker.

To determine which is the dominant season in setting the annual change, Fig. 6a shows the month of most extreme events based on the number of peaks over threshold for annual 1-yr returning event. The purple–blue colors along the U.S. West Coast indicate that DJF is the dominant period there, which is captured in all models (Figs. 6b–d). Despite large changes in the precipitation rate of the 1-yr returning event in other seasons along the U.S. West Coast, the annual mean

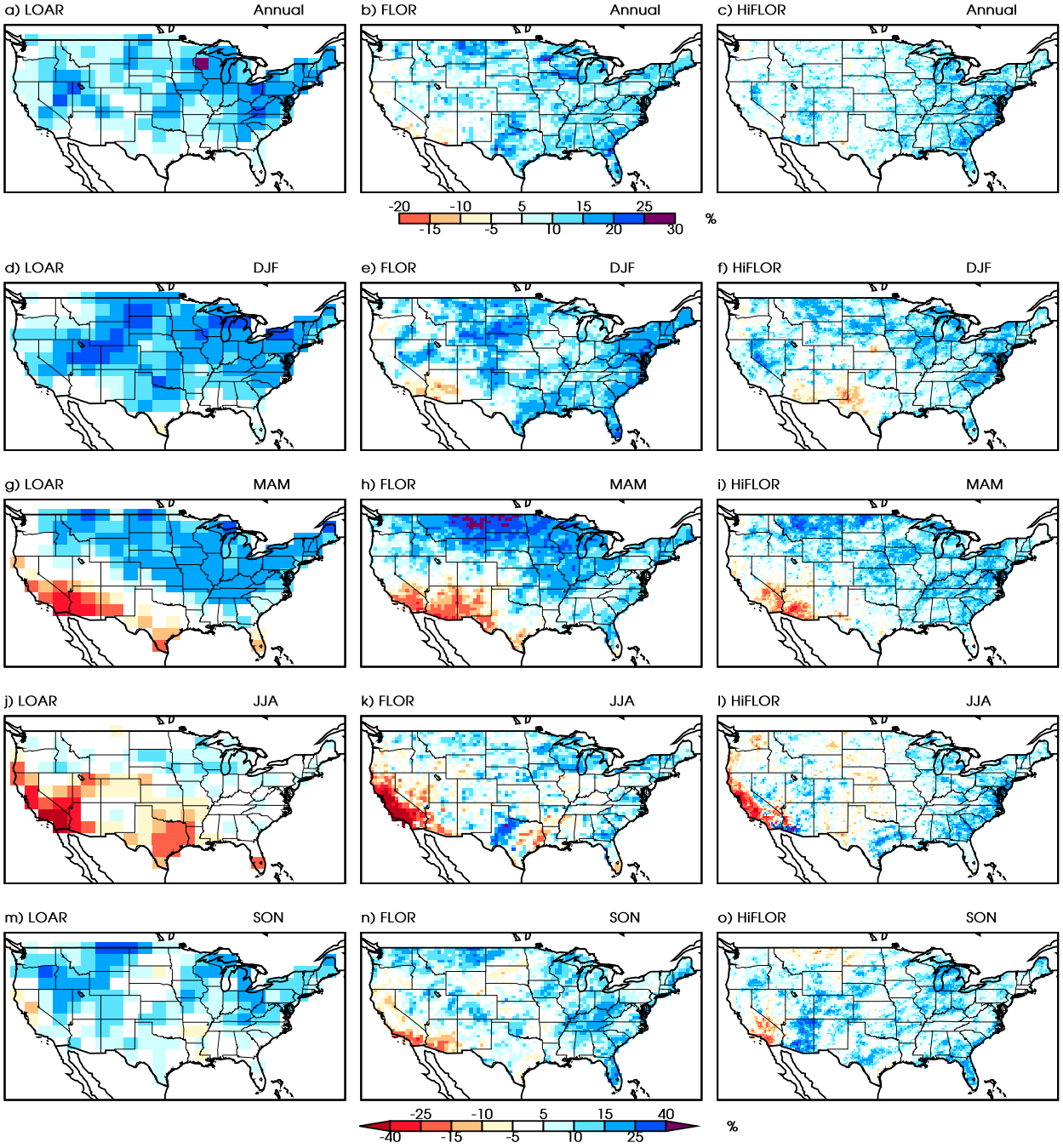

FIG. 5. As in Fig. 4, but for the relative increase of the precipitation rate of the 1-yr returning event of daily precipitation.

sensitivity (Figs. 5a–c) follows that of the DJF season (Figs. 5d–f).

In MAM (Figs. 5g–i) all models agree that the 1-yr returning event increases in intensity in the northern CONUS (locally $>12.5\%\,K^{-1}$) and decreases in intensity in parts of the southern CONUS. Decreasing extremes are found from California to Texas. If scaled to the local temperature change the decrease exceeds $12.5\%\,K^{-1}$ in LOAR and is weaker in higher-resolution models. Because the patterns are different in, for example, southern Texas (decreasing extremes in LOAR and FLOR and increasing extremes in HiFLOR), there must be different dynamical causes for these changes in the different models. The MAM season contributes toward setting the annual mean extreme event over the Great Plains (Fig. 6a). This contribution is not captured

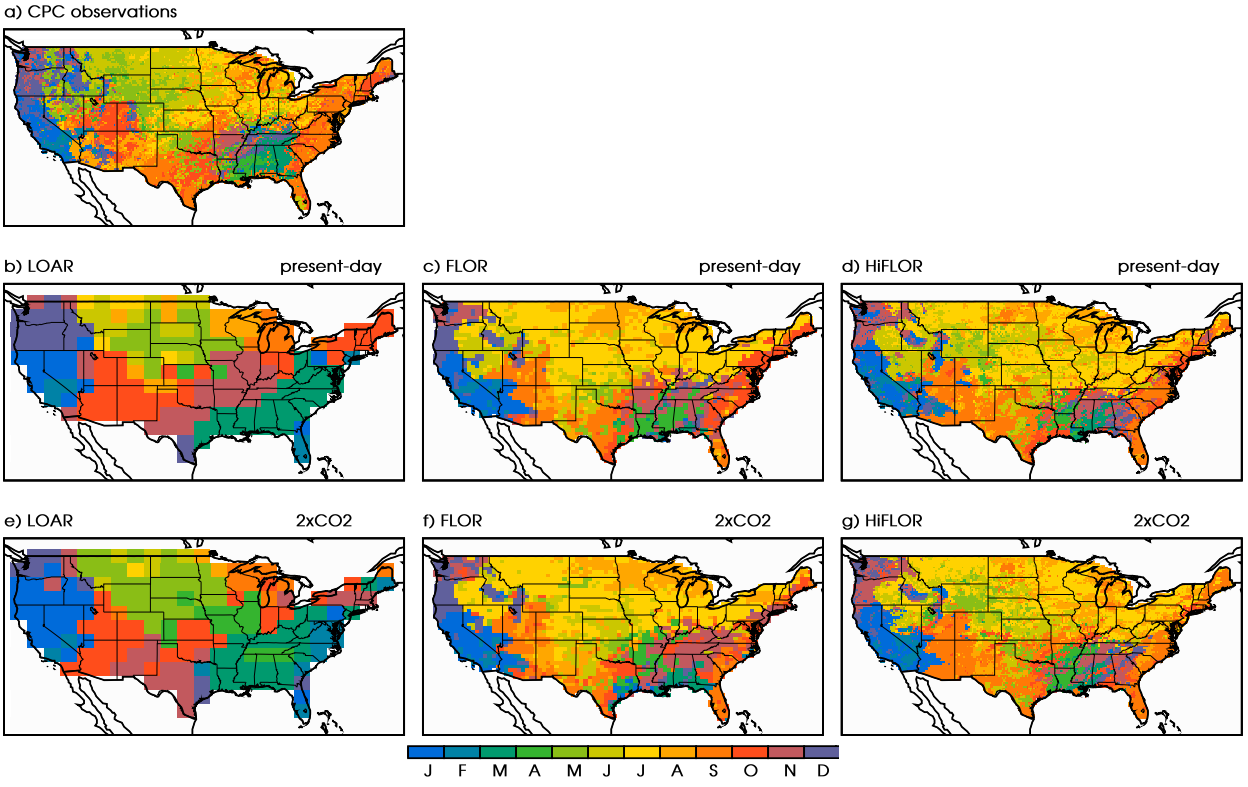

FIG. 6. Month with most peaks over threshold for the annual 1-yr returning event in (a) CPC observations, the present-day control experiment of (b) LOAR, (c) FLOR, and (d) HiFLOR, and in the $2 \times CO_2$ experiment of (e) LOAR, (f) FLOR, and (g) HiFLOR.

by FLOR and HiFLOR (Figs. 6b–d). LOAR correctly simulates MAM as the dominant season for the annual mean event over the Great Plains but is biased toward MAM in the Southeast (Fig. 6b).

Decreasing extreme precipitation rates are found over California during JJA in all models (Figs. 5j–l); if scaled to the model's temperature increase the decrease exceeds 12.5% K^{-1} in all models. Increasing precipitation rates associated with the 1-yr returning event are found near the Great Lakes (all models), in the Midwest (LOAR and FLOR), and along the Atlantic coast (FLOR and HiFLOR) and Gulf Coast (HiFLOR; >10% K^{-1}). The widespread decreasing mean precipitation in JJA (Figs. 4j–l) does not lead to widespread decreases in precipitation extremes.

The Atlantic coastal trends are also found in SON (Figs. 5m–o), particularly from Florida to South Carolina. Similar to JJA, these trends are only found in FLOR and HiFLOR (in places >10% K^{-1} in FLOR and HiFLOR); the amplitude is stronger in HiFLOR. Further increases in SON are found near the Great Lakes and the Midwest. Decreasing extremes are projected for California. The pattern is very different from the changes in mean precipitation in which large areas show decreasing precipitation (Figs. 4m–o).

Note that JJA and SON are part of the Atlantic hurricane season and that FLOR and HiFLOR are tropical cyclone-permitting models (Vecchi et al. 2014; Murakami et al. 2015). The changes noted in FLOR and HiFLOR along the Gulf and Atlantic coasts in those seasons, both vulnerable to tropical cyclones and hurricanes, may therefore be related to changes in tropical cyclone locations and/or frequencies. In fact, G. A. Vecchi et al. (2016, manuscript in preparation) shows that FLOR and HiFLOR exhibit a displacement of tropical cyclones from the Gulf of Mexico toward the Atlantic seaboard in response to $2 \times CO_2$. Such changes would not be captured in LOAR because of its coarse resolution. From Fig. 6a, it is clear that the hurricane season (especially the month of September) is a highly important season in setting the annual 1-yr returning event along the Atlantic coast. FLOR and HiFLOR, although they have a slight delay (Figs. 6c,d), reflect the influence of the hurricane season. LOAR does not successfully simulate the seasonality of extremes along the Atlantic coast; rather than the summer months, winter or early spring is the dominant time for precipitation extremes (Fig. 6b).

Although all models show significant changes in the intensity of the 1-yr returning event, changes in the seasonality of these extreme precipitation events are

minor. For example, along the Atlantic coast in FLOR extremes shift from October to September (Figs. 6c,f). LOAR shows larger shifts—for example, from November to March or April in the midlands (Figs. 6b,e). However, as discussed previously, there are large differences between the seasonality of the 1-yr returning event in LOAR and in the CPC data.

The CONUS mean change of the 5-yr/5-season returning event is larger than the change of the 1-yr/1-season returning event (Table 3). The patterns of change are approximately similar (Figs. 5 and 7); the local changes are stronger for the 5-yr/5-season returning event than for the 1-yr/1-season returning event. For example, along the South Atlantic coast the precipitation rate of the annual 5-yr returning event increases by >25% in HiFLOR (Fig. 7c). The same area shows positive changes for the annual 1-yr returning event, although slightly weaker (Fig. 5c). Local decreases of precipitation intensity in response to $2 \times CO_2$ forcing (e.g., in the Southwest in MAM; Figs. 5g–i) are weaker for the 5-season event.

c. *Trends in extreme precipitation in the observed record and historical experiments*

The projected changes in precipitation rates associated with the annual 1-yr returning event in response to $2 \times CO_2$ are substantial. Here we analyze observations and model simulations over the recent past to see if similar changes have already occurred. The mean trend of the frequency of the annual 1-yr returning event, as found in the CPC record, is shown in Fig. 8a. The CPC data show that the eastern CONUS has mostly experienced a positive trend (i.e., an increasing number) of extreme events, although there are intermittent grid points with a negative trend (i.e., a decreasing number of extreme events). In the western CONUS, positive and negative trends are found. The U.S. Northwest shows large negative trends that are not recovered by these models in a $2 \times CO_2$ climate (Figs. 5a–c). In some places the decrease exceeds two events per year every 100 years. If one considers that this is the trend of the frequency of the event with a mean return period of 1 yr over the 59 years for which CPC data are available, that must indicate that most qualifying events were in the first half of the record.

In Fig. 8d two time series of mean frequency of extreme events are shown, for those grid points in Fig. 8a that have the largest trends (Figs. 8b,c). Threshold values of plus or minus two events per year every 100 years have been chosen, which results in a selection of about 5% of the grid points in both cases. The line for grid points with a large negative trend verifies the sharp difference between the beginning and end of the record. Before 1978 there are on average 2.0 extreme events per year; in 1978 there is a sudden drop, after which the average number of events is $0.6\,yr^{-1}$. The change is smaller for the grid points with the large positive trend, from 0.6 events yr^{-1} before 1978 to 1.6 events yr^{-1} after 1978. Note that the mean value is not exactly equal to 1.0 because of the 3×3 box method used (see section 3). Besides climate change, two other possible mechanisms for this observed shift exist may be considered. First, in 1977 there was a shift in the Pacific decadal oscillation (PDO; Mantua and Hare 2002). The PDO impacts the CONUS hydroclimate (e.g., Hamlet and Lettenmaier 1999; Barlow et al. 2001; DeFlorio et al. 2013) and could therefore be responsible for the observed shift. A second explanation may be found in the nature of the gauge network over the CONUS. In the late 1970s and early 1980s a large number of automatic stations was added to the network, increasing the coverage over many sparsely covered areas. The effect of these changes on the consistency of interpolated and gridded precipitation products is unclear and bears examination given the coincidence of the timing of the observing system change and the extreme precipitation shifts. A similar analysis on two more temporally homogeneous data products is included in the appendix; one of these products is based on satellite data and is mostly independent from the gauge-based estimates. The pattern of trends is different between these products; none show the pattern that was found in the CPC data, despite the fact they cover the same time period.

Another way of investigating changes in the recent past is by looking at historical model integrations. Figures 9a,b show the ensemble mean trend in the historical experiment. There are large differences between the models; the ensemble of FLOR historical integrations show increasing numbers of extreme events in the Northeast and near the Great Lakes, and the rest of the CONUS shows both positive and negative trends without an obvious pattern. However, only 21% of the grid cells show an agreement of five or more (two-thirds) ensemble members with the sign of this trend (Fig. 9d). HiFLOR shows positive trends along the Canadian border but no pattern otherwise. In HiFLOR 23% of the grid has an agreement of five or more ensemble members (Fig. 9e). The ensemble mean of both models does not match the pattern that was found in the CPC record (Fig. 9c). There is a large variety of spatial patterns for the individual ensemble members (not shown), as can also be concluded from the low numbers in Figs. 9d,e.

The large differences between the trends as computed from model data and from the CPC record are of some concern. The difference between the pattern of Figs. 8a and 9c, based in part on the same data, raises the

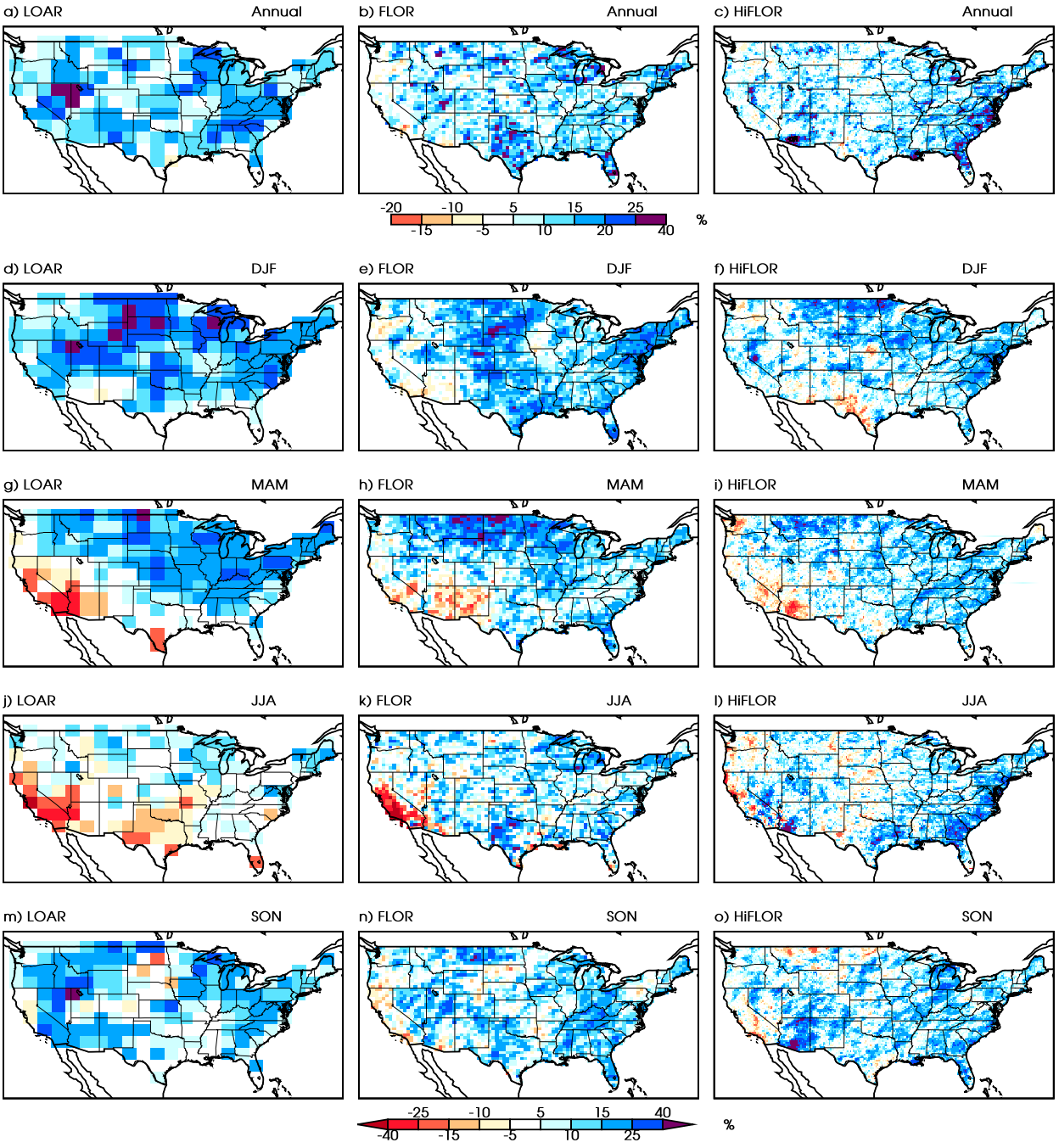

FIG. 7. As in Fig. 4, but for the relative increase of the precipitation rate of the 5-yr returning event of daily precipitation.

question whether the observational record is sufficiently long to make statements on the occurrence of extreme events. A 36-yr HiFLOR integration, in which SSTs are restored to a nonvarying annual cycle [Eq. (2)], shows that similar values of increasing or decreasing trends can be the result of internal variability alone (Fig. 9f).

Based on the presented data alone, it is not possible to conclude whether the models do not capture the observed changes, whether the trends in the CPC record are the result of changes in gauge distribution, or whether internal variability dominates over the forced climate change signal. The differences between FLOR and HiFLOR, the differences between individual ensemble members in the historical experiment, and the results of the HiFLOR climatological run suggest that the role of internal variability in setting the number of

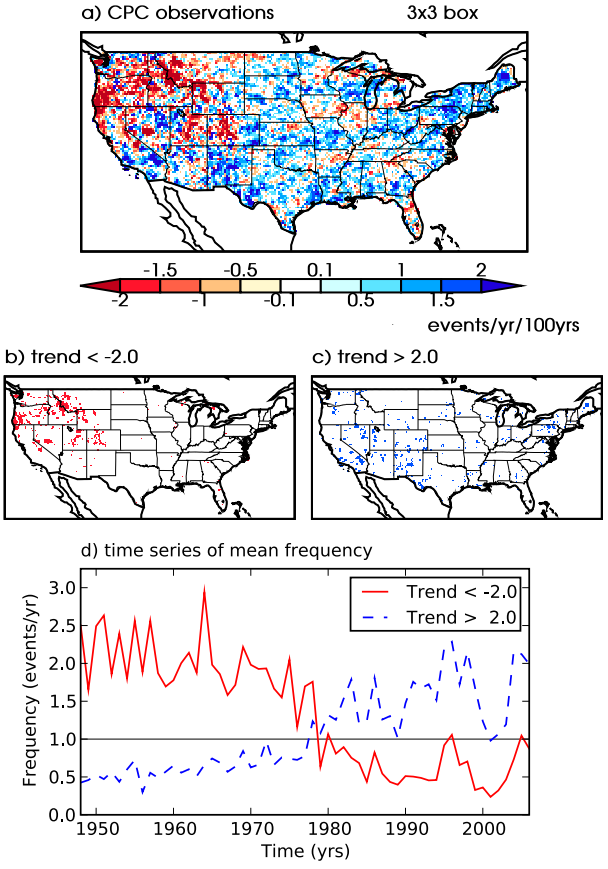

FIG. 8. (a) Observed trend of the frequency of the annual 1-yr returning event of daily precipitation [events yr^{-1} $(100\,yr)^{-1}$]. Trends were computed using the 3×3 box method over the period 1948–2006; only statistically significant trends (at the 5% level) are shown. (b) Locations where the trend is less than -2.0 events yr^{-1} $(100\,yr)^{-1}$ and (c) locations where the trend is greater than 2.0 events yr^{-1} $(100\,yr)^{-1}$. (d) Mean time series of event frequency for all grid points in (b) (red solid line) and for all grid points in (c) (blue dashed line).

extreme events is large and is larger than the forced signal over the period 1971–2012.

5. Summary and discussion

By means of experiments with a family of global coupled climate models with increasing atmospheric resolution, the nature of daily extreme precipitation events over the CONUS has been investigated. It has been shown that there is a consistent improvement of the quality of the simulated annual and seasonal mean precipitation with increasing horizontal resolution in the atmospheric model component. Additionally, the intensity, spatial pattern, and seasonality of precipitation extremes and the distribution of precipitation (light vs heavy) show consistent improvement. These results complement analyses of atmosphere-only models that noted similar improvements of mean and extreme precipitation with increasing resolution (Duffy et al. 2003; Iorio et al. 2004; Wehner et al. 2010).

In a $2 \times CO_2$ model experiment, the response of the mean precipitation, the 1-yr returning event and the 5-yr returning event of precipitation to global climate change is tested. The CONUS annual mean daily precipitation increases by 0.0%–0.8% K^{-1} in these models. The 1-yr returning event increases in intensity by 3.1%–4.1% K^{-1} and the 5-yr event by 3.7%–4.6% K^{-1}. Spatial pattern differences between models exist; changes are larger in the lower-resolution model. For individual seasons, differences between models become more obvious. For example, in the higher-resolution, tropical-cyclone-permitting models (FLOR and HiFLOR), the Atlantic coast from North Carolina to Florida is a hotspot for change in the summer months. The low-resolution model (LOAR) does not project any change in extreme precipitation intensity for the same period and location. It is hypothesized that changes in tropical cyclone frequency, precipitation, and location may be responsible for the southeastern CONUS changes in FLOR and HiFLOR. LOAR has a too-coarse resolution to simulate tropical cyclones and is therefore unable to simulate the extreme events associated with tropical cyclones correctly and cannot project associated changes in a reliable manner.

It was previously known that there is a minimum model resolution that is required to capture the weather phenomena that lead to precipitation extremes, for example, by orographic-forced precipitation (e.g., Kapnick and Delworth 2013) or tropical-cyclone-induced precipitation (e.g., Murakami et al. 2015). However, the results presented here show that it is important to meet that minimum resolution when making climate change projections. The authors therefore recommend that, for any study of climate change, a careful consideration of the minimum required model resolution for the specific scientific problem is done. An interesting question to ask is whether downscaling LOAR data would give the same results obtained by FLOR and HiFLOR or whether results based on high-resolution coupled models such as FLOR or HiFLOR are fundamentally different from downscaling experiments.

Statistically significant trends in the frequency of extreme precipitation events exist in the observed record. However, based on differences between the observed record and historical model experiments, differences between observational products, and differences between individual ensemble members in the historical experiment, at this moment, those cannot be attributed to climate change alone. The authors acknowledge this creates a difficult situation for interpreting the past and

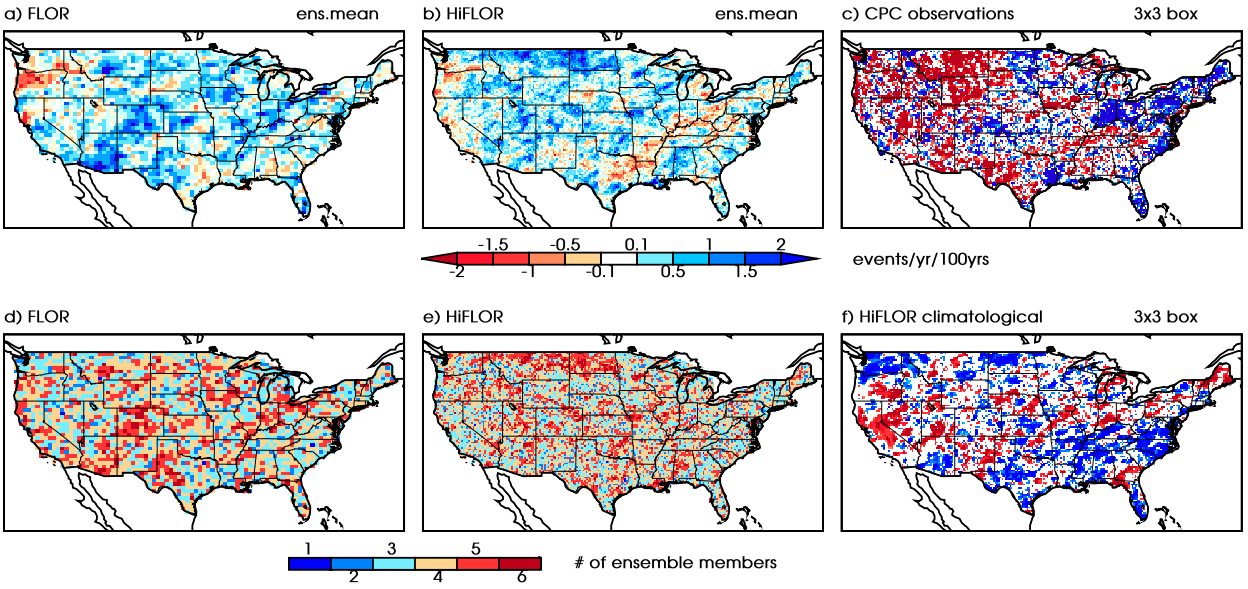

FIG. 9. (a),(b) Ensemble mean trend of the annual 1-yr returning event of daily precipitation in the historical experiment [events yr^{-1} $(100\ yr)^{-1}$]. Trends computed using the one-gridpoint method over the period 1971–2006. (c) As in Fig. 8a, but for the period 1971–2006. (d),(e) Number of ensemble members that have the same sign of the trend as the ensemble mean trend shown in (a),(b). (f) As in (c), but for a 36-yr HiFLOR integration restored to a yearly repeating SST climatology. Note that (c) and (f) use the same color bar as (a) and (b). Models shown are (a),(d) FLOR and (b),(e),(f) HiFLOR.

assessing predictions of the future: based on model experiments the intensity and frequency of extreme precipitation events are predicted to increase in response to increasing CO_2 concentrations; however, these same models suggest that, because of substantial internal variability, the observed record is too short to make statements on whether these changes have already started to occur in the natural environment.

Besides extreme precipitation, there are many other aspects of climate and climate change that are worth revisiting with these newly developed coupled models, such as the change in global climate sensitivity (temperature change following a doubling of atmospheric CO_2) as noted here and in G. A. Vecchi et al. (2016, manuscript in preparation). Furthermore, the high atmospheric resolution now allows for the direct investigation of regional climate phenomena in a global coupled model framework. For example, a detailed study of the circulation changes associated with the noted change in precipitation extremes along the Atlantic coast in FLOR and HiFLOR is under way. The hypothesized attribution of these precipitation changes to changes in tropical cyclones is being further investigated. The present study may be extended by considering the impact of increasing vertical resolution in the atmospheric model component.

Finally, it should be noted that the quality of climate models can only be verified by comparing against observational datasets. It is therefore of high importance that reliable observational data products, covering an extensive time period, exist. Despite the CONUS having a relatively high density of gauge stations compared to other regions globally, there are areas with relatively few gauges and biased observations as a consequence. Such biases are found in particular over complex terrain (e.g., Lundquist et al. 2015), where much of the precipitation characteristics are still waiting to be fully understood. Furthermore, the coincidence of the observed changes in extreme precipitation with changes in gauge distributions brings to the fore the need for a systematic evaluation of the impact of observing system changes on our estimates of changes in extreme precipitation.

Acknowledgments. The authors thank Vaishali Naik and Ángel G. Muñoz for helpful reviews of an earlier draft. The authors thank three anonymous reviewers for their comments, which helped to improve the manuscript. Funding for this work was supplied by the U.S. Department of Commerce National Oceanic and Atmospheric Administration to the Geophysical Fluid Dynamics Laboratory, to the Cooperative Institute for Climate Science (Award NA14OAR4320106), and to the University Corporation for Atmospheric Research. The statements, findings, conclusions, and recommendations are those of the author(s) and do not necessarily reflect the views of the National Oceanic and Atmospheric Administration or the U.S. Department of

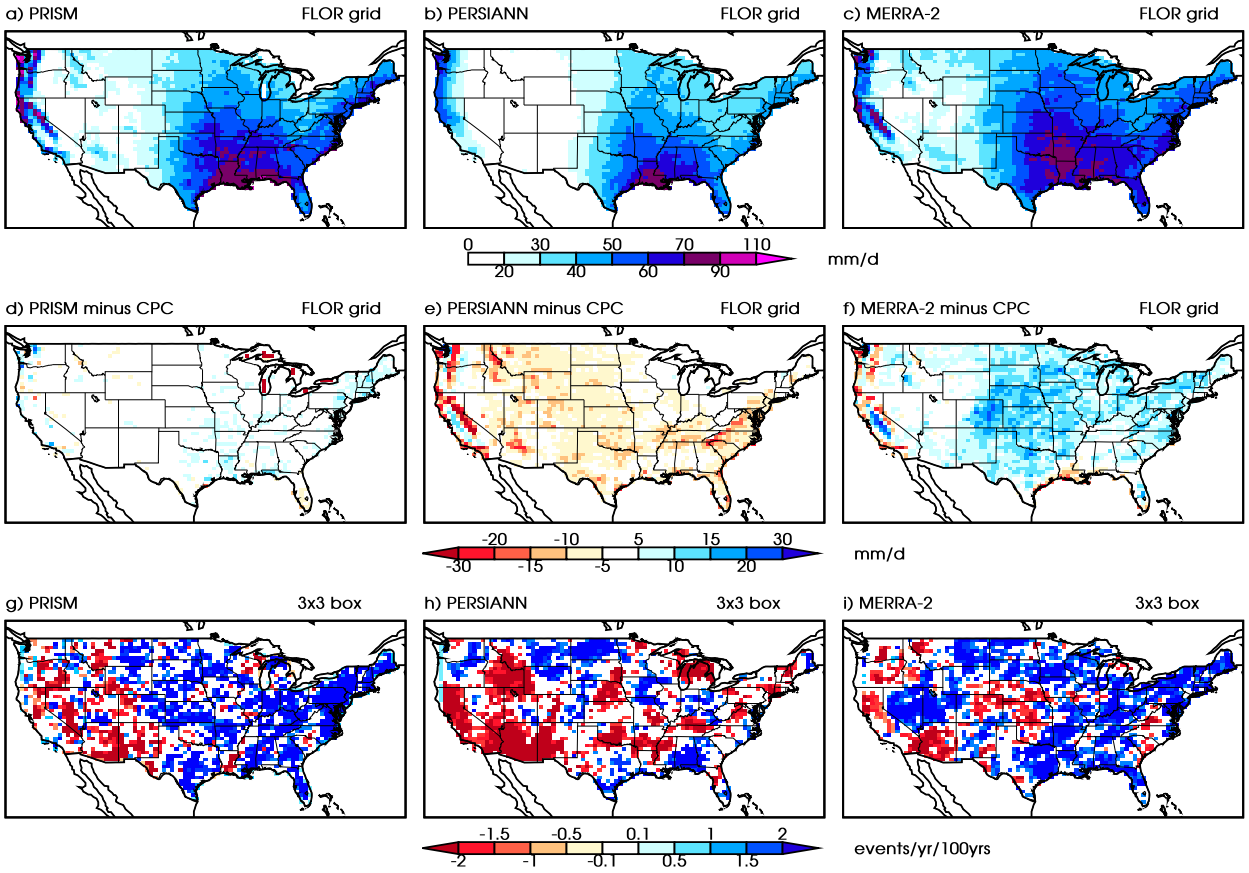

FIG. A1. The 1-yr returning event of daily precipitation rate (mm day^{-1}) on the FLOR grid as in Fig. 2b, but for (a) PRISM, (b) PERSIANN, and (c) MERRA-2 data. Differences between tested datasets and the CPC product (mm day^{-1}) on the FLOR grid for (d) PRISM, (e) PERSIANN, and (f) MERRA-2 data. Note the color scale is similar to that used for Figs. 2d–i. Trend of the frequency of the annual 1-yr returning event of daily precipitation [events yr^{-1} (100 yr)$^{-1}$] as in Figs. 8a and 9c, but for (g) PRISM, (h) PERSIANN, and (i) MERRA-2 data.

Commerce. CPC U.S. unified precipitation data were provided by the NOAA/OAR/ESRL PSD, Boulder, Colorado, from their website (http://www.esrl.noaa.gov/psd/data/gridded/data.unified.daily.conus.html). PRISM data were provided by PRISM Climate Group, Oregon State University, Corvallis, Oregon, from their website (http://www.prism.oregonstate.edu). PERSIANN-CDR data were provided by the NOAA/NESDIS/NCEI, Asheville, North Carolina, from their download site (ftp://eclipse.ncdc.noaa.gov/). MERRA-2 data were provided by the NASA/GEC/DISC, Greenbelt, Maryland, from their website (http://disc.sci.gsfc.nasa.gov/daac-bin/FTPSubset2.pl).

APPENDIX

Comparison of Observational Data Products for Extreme Precipitation

Biases in observational-based estimates of precipitation influence the evaluation of model simulated precipitation (as done in Section 4a) and the analysis of trends in such datasets (as in Section 4c). Reliable estimates of precipitation extremes and trends therein require datasets to span long periods, such that the extreme events can be sampled adequately, and require datasets to be homogeneous. The CPC dataset that was used for verification and in the analysis here spans 59 years, but might not be homogeneous because of changes in gauge observation (section 4c; Fig. 8d). Here three additional datasets are used to compare CPC-based estimates of the 1-yr and 5-yr returning event, estimates of trends of the frequency of the 1-yr returning event and to further verify model output.

The additional products were selected to cover a range of data sources. The PRISM data (Daly et al. 2008; 4 km × 4 km resolution, 1981–2012) is a gauge-based dataset, although its interpolation method is more complex than that of the CPC data because it takes into account local physiographic information.

TABLE A1. As in Table 2, for the annual 1- and 5-yr returning events (mm day^{-1}), but for intercomparing observational products.

Dataset	Grid	Mean	Bias	RMSE	Corr
			1-yr returning event		
CPC	FLOR	39.04	—	—	—
PRISM	FLOR	40.01	0.97	4.51	0.97
PERSIANN	FLOR	32.86	−6.18	8.68	0.93
MERRA-2	FLOR	45.36	6.32	9.56	0.91
			5-yr returning event		
CPC	FLOR	57.83	—	—	—
PRISM	FLOR	58.87	1.05	8.19	0.96
PERSIANN	FLOR	47.08	−10.75	14.69	0.92
MERRA-2	FLOR	66.82	8.99	15.05	0.88

PERSIANN data (Hsu et al. 1997; 0.25° × 0.25° resolution, 1983–2015) is a daily satellite product. It is adjusted to GPCP version 2.2 data at monthly time scales, it is therefore not completely independent from the gauge-based observational data. Finally the reanalysis product MERRA-2 (Bosilovich et al. 2015; Rienecker et al. 2011; 0.5° × 0.667° resolution, 1980–2015) was selected. Disadvantages of PERSIANN and MERRA-2 data include their dependence on indirect measurements of precipitation, however these products are temporally more homogeneous data than the CPC or PRISM data. All of the selected additional products span a shorter time period than the CPC data.

The pattern of precipitation rates associated with the 1-yr returning event is comparable in all datasets (Figs. 2b and A1a–c). Pattern correlations exceed 0.9 for all datasets (Table A1). PRISM data is closest to CPC data, although the PRISM data doesn't interpolate station data to cover the Great Lakes (where no stations exist) as CPC does. There is no clear difference over mountainous regions, as might be expected from the increased complexity of the PRISM interpolation algorithm. PERSIANN data has weaker precipitation rates associated with the 1-yr returning event than the CPC data, MERRA-2 shows stronger precipitation rates (Figs. A1d–f). Biases and RMSEs when compared to CPC are much larger in the PERSIANN data and MERRA-2 than in the PRISM data (Table A1). These differences between datasets are the same for the 5-yr returning event.

The verification of modeled precipitation rates for the 1-yr returning event (Table 2) is repeated here for the selected data products. As was found for the CPC data, comparison against PRISM data shows a consequent improvement of simulated precipitation rates with increasing horizontal resolution (Table A2). Comparison against PERSIANN data shows HiFLOR performs well when all models are compared at the LOAR grid. At the FLOR grid, FLOR has a slightly higher pattern correlation than HiFLOR does. The comparison against MERRA-2 gives different results and indicates FLOR outperforms HiFLOR for all quantities measured. Note that precipitation in MERRA-2 and other reanalysis products is a modeled field, constrained by a correct dynamical atmospheric state. It depends therefore on parameterization schemes, which potentially introduces biases very similar to those in the model output.

TABLE A2. As in Table 2 for the annual 1-yr returning event (mm day^{-1}), but comparing against different observational products.

Model or dataset	Grid	Mean	Bias	RMSE	Corr
			PRISM		
PRISM	LOAR	33.54	—	—	—
LOAR	LOAR	35.60	2.06	8.49	0.86
FLOR	LOAR	36.69	3.15	7.21	0.91
HiFLOR	LOAR	34.05	**0.51**	**5.78**	**0.93**
PRISM	FLOR	40.01	—	—	—
FLOR	FLOR	45.02	5.01	11.47	0.85
HiFLOR	FLOR	42.59	**2.59**	**8.93**	**0.89**
			PERSIANN		
PERSIANN	LOAR	29.62	—	—	—
LOAR	LOAR	35.60	5.98	10.27	0.84
FLOR	LOAR	36.69	7.07	10.02	0.88
HiFLOR	LOAR	34.05	**4.43**	**7.81**	**0.90**
PERSIANN	FLOR	32.86	—	—	—
FLOR	FLOR	45.02	12.16	14.92	**0.84**
HiFLOR	FLOR	42.59	**9.74**	**12.58**	0.87
			MERRA-2		
MERRA-2	LOAR	37.61	—	—	—
LOAR	LOAR	35.60	−2.01	6.88	0.89
FLOR	LOAR	36.69	**0.92**	**5.31**	**0.92**
HiFLOR	LOAR	34.05	−3.56	6.62	0.91
MERRA-2	FLOR	45.36	—	—	—
FLOR	FLOR	45.02	**−0.34**	**7.37**	**0.91**
HiFLOR	FLOR	42.59	−2.76	7.60	0.90

Finally, we show the trend of the frequency of the 1-yr returning event in the three data products (Figs. A1g–i). These estimates of trends in extreme precipitation are similar to those shown in Fig. 8a or Fig. 9c (the latter based on a shorter time period, similar to those shown here). The patterns of the trend are different in each data product, verifying the conclusion based on the model experiments that the observational record is too short for such analysis. The two temporally more homogenous products (PERSIANN and MERRA-2 data) do not show any agreement on the sign of the trend in different CONUS regions. For example, in MERRA-2 the U.S. Northeast is shown to have stronger extremes, in the PERSIANN data this area sees no significant change or change of the opposite sign.

REFERENCES

Allen, M. R., and W. J. Ingram, 2002: Constraints on future changes in climate and the hydrologic cycle. *Nature*, **419**, 224–232, doi:10.1038/nature01092.

Anderson, J. L., and Coauthors, 2004: The new GFDL global atmosphere and land model AM2–LM2: Evaluation with prescribed SST simulations. *J. Climate*, **17**, 4641–4673, doi:10.1175/JCLI-3223.1.

Barlow, M., S. Nigam, and E. Berbery, 2001: ENSO, Pacific decadal variability, and U.S. summertime precipitation, drought, and stream flow. *J. Climate*, **14**, 2105–2128, doi:10.1175/1520-0442(2001)014<2105:EPDVAU>2.0.CO;2.

Bosilovich, M. G., and Coauthors, 2015: MERRA-2: Initial evaluation of the climate. NASA Tech. Rep. Series on Global Modeling and Data Assimilation 43, 139 pp. [Available online at https://gmao.gsfc.nasa.gov/pubs/tm/docs/Bosilovich803.pdf.]

Chen, C.-T., and T. Knutson, 2008: On the verification and comparison of extreme rainfall indices from climate models. *J. Climate*, **21**, 1605–1621, doi:10.1175/2007JCLI1494.1.

Chen, M., W. Shi, P. Xie, V. Silva, V. E. Kousky, R. Wayne Higgins, and J. E. Janowiak, 2008: Assessing objective techniques for gauge-based analyses of global daily precipitation. *J. Geophys. Res.*, **113**, D04110, doi:10.1029/2007JD009132.

Curriero, F. C., J. A. Patz, J. B. Rose, and S. Lele, 2001: The association between extreme precipitation and waterborne disease outbreaks in the United States, 1948–1994. *Amer. J. Public Health*, **91**, 1194–1199, doi:10.2105/AJPH.91.8.1194.

Dai, A., 2006: Precipitation characteristics in eighteen coupled climate models. *J. Climate*, **19**, 4605–4630, doi:10.1175/JCLI3884.1.

Daly, C., M. Halbleib, J. I. Smith, W. P. Gibson, M. K. Doggett, G. H. Taylor, J. Curtis, and P. P. Pasteris, 2008: Physiographically sensitive mapping of climatological temperature and precipitation across the conterminous United States. *Int. J. Climatol.*, **28**, 2031–2064, doi:10.1002/joc.1688.

DeFlorio, M. J., D. W. Pierce, D. R. Cayan, and A. J. Miller, 2013: Western U.S. extreme precipitation events and their relation to ENSO and PDO in CCSM4. *J. Climate*, **26**, 4231–4243, doi:10.1175/JCLI-D-12-00257.1.

Delworth, T. L., and Coauthors, 2006: GFDL's CM2 global coupled climate models. Part I: Formulation and simulation characteristics. *J. Climate*, **19**, 643–674, doi:10.1175/JCLI3629.1.

——, and Coauthors, 2012: Simulated climate and climate change in the GFDL CM2.5 high-resolution coupled climate model. *J. Climate*, **25**, 2755–2781, doi:10.1175/JCLI-D-11-00316.1.

Dibike, Y. B., and P. Coulibaly, 2006: Temporal neural networks for downscaling climate variability and extremes. *Neural Netw.*, **19**, 135–144, doi:10.1016/j.neunet.2006.01.003.

Duffy, P., B. Govindasamy, J. Iorio, J. Milovich, K. Sperber, K. Taylor, M. Wehner, and S. Thompson, 2003: High-resolution simulations of global climate, part 1: Present climate. *Climate Dyn.*, **21**, 371–390, doi:10.1007/s00382-003-0339-z.

Durman, C., J. M. Gregory, D. C. Hassell, R. Jones, and J. Murphy, 2001: A comparison of extreme European daily precipitation simulated by a global and a regional climate model for present and future climates. *Quart. J. Roy. Meteor. Soc.*, **127**, 1005–1015, doi:10.1002/qj.49712757316.

Fay, P. A., J. D. Carlisle, A. K. Knapp, J. M. Blair, and S. L. Collins, 2003: Productivity responses to altered rainfall patterns in a C4-dominated grassland. *Oecologia*, **137**, 245–251, doi:10.1007/s00442-003-1331-3.

Fischer, E. M., and R. Knutti, 2015: Anthropogenic contribution to global occurrence of heavy-precipitation and high-temperature extremes. *Nat. Climate Change*, **5**, 560–564, doi:10.1038/nclimate2617.

Frei, C., R. Schöll, S. Fukutome, J. Schmidli, and P. L. Vidale, 2006: Future change of precipitation extremes in Europe: Intercomparison of scenarios from regional climate models. *J. Geophys. Res.*, **111**, D06105, doi:10.1029/2005JD005965.

Gandin, L. S., and R. Hardin, 1965: *Objective Analysis of Meteorological Fields*. Israel Program for Scientific Translation, 242 pp.

Griffies, S. M., 2012: Elements of the Modular Ocean Model (MOM). NOAA/Geophysical Fluid Dynamics Laboratory Tech. Rep. 7, 614 pp.

Groisman, P. Ya., R. W. Knight, and T. R. Karl, 2001: Heavy precipitation and high streamflow in the contiguous United States: Trends in the twentieth century. *Bull. Amer. Meteor. Soc.*, **82**, 219–246, doi:10.1175/1520-0477(2001)082<0219:HPAHSI>2.3.CO;2.

Gutowski, W. J., Jr., and Coauthors, 2010: Regional extreme monthly precipitation simulated by NARCCAP RCMs. *J. Hydrometeor.*, **11**, 1373–1379, doi:10.1175/2010JHM1297.1.

Hamlet, A. F., and D. P. Lettenmaier, 1999: Columbia River streamflow forecasting based on ENSO and PDO climate signals. *J. Water Resour. Plann. Manage.*, **125**, 333–341, doi:10.1061/(ASCE)0733-9496(1999)125:6(333).

Higgins, R. W., W. Shi, E. Yarosh, and R. Joyce, 2000: Improved United States precipitation quality control system and analysis. NCEP/Climate Prediction Center Atlas 7. [Available online at http://www.cpc.ncep.noaa.gov/research_papers/ncep_cpc_atlas/7/toc.html.]

Hsu, K.-L., X. Gao, S. Sorooshian, and H. Gupta, 1997: Precipitation estimation from remotely sensed information using artificial neural networks. *J. Appl. Meteor.*, **36**, 1176–1190, doi:10.1175/1520-0450(1997)036<1176:PEFRSI>2.0.CO;2.

Iorio, J., P. Duffy, B. Govindasamy, S. Thompson, M. Khairoutdinov, and D. Randall, 2004: Effects of model resolution and subgrid-scale physics on the simulation of precipitation in the continental United States. *Climate Dyn.*, **23**, 243–258, doi:10.1007/s00382-004-0440-y.

IPCC, 2007: *Climate Change 2007: The Physical Science Basis*. Cambridge University Press, 996 pp.

——, 2013: *Climate Change 2013: The Physical Science Basis*. Cambridge University Press, 1535 pp., doi:10.1017/CBO9781107415324.

Jackson, R. B., S. R. Carpenter, C. N. Dahm, D. M. McKnight, R. J. Naiman, S. L. Postel, and S. W. Running, 2001: Water in a changing world. *Ecol. Appl.*, **11**, 1027–1045, doi:10.1890/1051-0761(2001)011[1027:WIACW]2.0.CO;2.

Jia, L., and Coauthors, 2015: Improved seasonal prediction of temperature and precipitation over land in a high-resolution GFDL climate model. *J. Climate*, **28**, 2044–2062, doi:10.1175/JCLI-D-14-00112.1.

Kapnick, S. B., and T. L. Delworth, 2013: Controls of global snow under a changed climate. *J. Climate*, **26**, 5537–5562, doi:10.1175/JCLI-D-12-00528.1.

——, ——, M. Ashfaq, S. Malyshev, and P. Milly, 2014: Snowfall less sensitive to warming in Karakoram than in Himalayas due to a unique seasonal cycle. *Nat. Geosci.*, **7**, 834–840, doi:10.1038/ngeo2269.

Kharin, V. V., F. W. Zwiers, X. Zhang, and G. C. Hegerl, 2007: Changes in temperature and precipitation extremes in the IPCC ensemble of global coupled model simulations. *J. Climate*, **20**, 1419–1444, doi:10.1175/JCLI4066.1.

——, F. Zwiers, X. Zhang, and M. Wehner, 2013: Changes in temperature and precipitation extremes in the CMIP5

ensemble. *Climatic Change*, **119**, 345–357, doi:10.1007/s10584-013-0705-8.

Knapp, A. K., and Coauthors, 2008: Consequences of more extreme precipitation regimes for terrestrial ecosystems. *BioScience*, **58**, 811–821, doi:10.1641/B580908.

Kunkel, K. E., 2003: North American trends in extreme precipitation. *Nat. Hazards*, **29**, 291–305, doi:10.1023/A:1023694115864.

——, K. Andsager, and D. R. Easterling, 1999: Long-term trends in extreme precipitation events over the conterminous United States and Canada. *J. Climate*, **12**, 2515–2527, doi:10.1175/1520-0442(1999)012<2515:LTTIEP>2.0.CO;2.

Lee, J.-E., R. Pierrehumbert, A. Swann, and B. R. Lintner, 2009: Sensitivity of stable water isotopic values to convective parameterization schemes. *Geophys. Res. Lett.*, **36**, L23801, doi:10.1029/2009GL040880.

Lundquist, J. D., M. Hughes, B. Henn, E. D. Gutmann, B. Livneh, J. Dozier, and P. Neiman, 2015: High-elevation precipitation patterns: Using snow measurements to assess daily gridded datasets across the Sierra Nevada, California. *J. Hydrometeor.*, **16**, 1773–1792, doi:10.1175/JHM-D-15-0019.1.

Mallakpour, I., and G. Villarini, 2015: The changing nature of flooding across the central United States. *Nat. Climate Change*, **5**, 250–254, doi:10.1038/nclimate2516.

Maloney, E. D., and Coauthors, 2014: North American climate in CMIP5 experiments. Part III: Assessment of twenty-first-century projections. *J. Climate*, **27**, 2230–2270, doi:10.1175/JCLI-D-13-00273.1.

Mantua, N. J., and S. R. Hare, 2002: The Pacific decadal oscillation. *J. Oceanogr.*, **58**, 35–44, doi:10.1023/A:1015820616384.

Mehran, A., A. AghaKouchak, and T. Phillips, 2014: Evaluation of CMIP5 continental precipitation simulations relative to satellite-based gauge-adjusted observations. *J. Geophys. Res. Atmos.*, **119**, 1695–1707, doi:10.1002/2013JD021152.

Milly, P., and Coauthors, 2014: An enhanced model of land water and energy for global hydrologic and earth-system studies. *J. Hydrometeor.*, **15**, 1739–1761, doi:10.1175/JHM-D-13-0162.1.

Min, S.-K., X. Zhang, F. W. Zwiers, and G. C. Hegerl, 2011: Human contribution to more-intense precipitation extremes. *Nature*, **470**, 378–381, doi:10.1038/nature09763.

Msadek, R., G. Vecchi, M. Winton, and R. Gudgel, 2014: Importance of initial conditions in seasonal predictions of Arctic sea ice extent. *Geophys. Res. Lett.*, **41**, 5208–5215, doi:10.1002/2014GL060799.

Muller, C. J., P. A. O'Gorman, and L. E. Back, 2011: Intensification of precipitation extremes with warming in a cloud-resolving model. *J. Climate*, **24**, 2784–2800, doi:10.1175/2011JCLI3876.1.

Murakami, H., and Coauthors, 2015: Simulation and prediction of category 4 and 5 hurricanes in the high-resolution GFDL HiFLOR coupled climate model. *J. Climate*, **28**, 9058–9079, doi:10.1175/JCLI-D-15-0216.1.

Ning, L., E. E. Riddle, and R. S. Bradley, 2015: Projected changes in climate extremes over the northeastern United States. *J. Climate*, **28**, 3289–3310, doi:10.1175/JCLI-D-14-00150.1.

O'Gorman, P. A., 2015: Precipitation extremes under climate change. *Curr. Climate Change Rep.*, **1**, 49–59, doi:10.1007/s40641-015-0009-3.

——, and T. Schneider, 2009: The physical basis for increases in precipitation extremes in simulations of 21st-century climate change. *Proc. Natl. Acad. Sci. USA*, **106**, 14 773–14 777, doi:10.1073/pnas.0907610106.

Pall, P., M. Allen, and D. Stone, 2007: Testing the Clausius–Clapeyron constraint on changes in extreme precipitation under CO_2 warming. *Climate Dyn.*, **28**, 351–363, doi:10.1007/s00382-006-0180-2.

Peterson, T. C., X. Zhang, M. Brunet-India, and J. L. Vázquez-Aguirre, 2008: Changes in North American extremes derived from daily weather data. *J. Geophys. Res.*, **113**, D07113, doi:10.1029/2007JD009453.

Pielke, R. A., Jr., and M. W. Downton, 2000: Precipitation and damaging floods: Trends in the United States, 1932–97. *J. Climate*, **13**, 3625–3637, doi:10.1175/1520-0442(2000)013<3625:PADFTI>2.0.CO;2.

Putman, W. M., and S.-J. Lin, 2007: Finite-volume transport on various cubed-sphere grids. *J. Comput. Phys.*, **227**, 55–78, doi:10.1016/j.jcp.2007.07.022.

Rayner, N., D. E. Parker, E. Horton, C. Folland, L. Alexander, D. Rowell, E. Kent, and A. Kaplan, 2003: Global analyses of sea surface temperature, sea ice, and night marine air temperature since the late nineteenth century. *J. Geophys. Res.*, **108**, 4407, doi:10.1029/2002JD002670.

Rienecker, M. M., and Coauthors, 2011: MERRA: NASA's Modern-Era Retrospective Analysis for Research and Applications. *J. Climate*, **24**, 3624–3648, doi:10.1175/JCLI-D-11-00015.1.

Rosenzweig, C., F. N. Tubiello, R. Goldberg, E. Mills, and J. Bloomfield, 2002: Increased crop damage in the US from excess precipitation under climate change. *Global Environ. Change*, **12**, 197–202, doi:10.1016/S0959-3780(02)00008-0.

Schoof, J. T., 2015: High-resolution projections of 21st century daily precipitation for the contiguous US. *J. Geophys. Res. Atmos.*, **120**, 3029–3042, doi:10.1002/2014JD022376.

——, and S. M. Robeson, 2016: Projecting changes in regional temperature and precipitation extremes in the United States. *Wea. Climate Extremes*, **11**, 28–40, doi:10.1016/j.wace.2015.09.004.

Schubert, S. D., Y. Chang, M. J. Suarez, and P. J. Pegion, 2008: ENSO and wintertime extreme precipitation events over the contiguous United States. *J. Climate*, **21**, 22–39, doi:10.1175/2007JCLI1705.1.

Sen Roy, S., and R. C. Balling, 2004: Trends in extreme daily precipitation indices in India. *Int. J. Climatol.*, **24**, 457–466, doi:10.1002/joc.995.

Sheffield, J., and Coauthors, 2013: North American climate in CMIP5 experiments. Part I: Evaluation of historical simulations of continental and regional climatology. *J. Climate*, **26**, 9209–9245, doi:10.1175/JCLI-D-12-00592.1.

Shiu, C.-J., S. C. Liu, C. Fu, A. Dai, and Y. Sun, 2012: How much do precipitation extremes change in a warming climate? *Geophys. Res. Lett.*, **39**, L17707, doi:10.1029/2012GL052762.

Sillmann, J., V. Kharin, F. Zwiers, X. Zhang, and D. Bronaugh, 2013: Climate extremes indices in the CMIP5 multimodel ensemble: Part 2. Future climate projections. *J. Geophys. Res. Atmos.*, **118**, 2473–2493, doi:10.1002/jgrd.50188.

Stock, C. A., and Coauthors, 2015: Seasonal sea surface temperature anomaly prediction for coastal ecosystems. *Prog. Oceanogr.*, **137**, 219–236, doi:10.1016/j.pocean.2015.06.007.

Sun, Y., S. Solomon, A. Dai, and R. W. Portmann, 2007: How often will it rain? *J. Climate*, **20**, 4801–4818, doi:10.1175/JCLI4263.1.

Thibeault, J. M., and A. Seth, 2014: Changing climate extremes in the northeast United States: Observations and projections from CMIP5. *Climatic Change*, **127**, 273–287, doi:10.1007/s10584-014-1257-2.

Toreti, A., and Coauthors, 2013: Projections of global changes in precipitation extremes from Coupled Model Intercomparison

Project phase 5 models. *Geophys. Res. Lett.*, **40**, 4887–4892, doi:10.1002/grl.50940.

Trenberth, K. E., A. Dai, R. M. Rasmussen, and D. B. Parsons, 2003: The changing character of precipitation. *Bull. Amer. Meteor. Soc.*, **84**, 1205–1217, doi:10.1175/BAMS-84-9-1205.

Vecchi, G. A., and Coauthors, 2014: On the seasonal forecasting of regional tropical cyclone activity. *J. Climate*, **27**, 7994–8016, doi:10.1175/JCLI-D-14-00158.1.

Villarini, G., E. Scoccimarro, and S. Gualdi, 2013a: Projections of heavy rainfall over the central United States based on CMIP5 models. *Atmos. Sci. Lett.*, **14**, 200–205, doi:10.1002/asl2.440.

——, J. A. Smith, and G. A. Vecchi, 2013b: Changing frequency of heavy rainfall over the central United States. *J. Climate*, **26**, 351–357, doi:10.1175/JCLI-D-12-00043.1.

Wehner, M. F., R. L. Smith, G. Bala, and P. Duffy, 2010: The effect of horizontal resolution on simulation of very extreme US precipitation events in a global atmosphere model. *Climate Dyn.*, **34**, 241–247, doi:10.1007/s00382-009-0656-y.

Westra, S., and Coauthors, 2014: Future changes to the intensity and frequency of short-duration extreme rainfall. *Rev. Geophys.*, **52**, 522–555, doi:10.1002/2014RG000464.

Wuebbles, D., and Coauthors, 2014: CMIP5 climate model analyses: Climate extremes in the United States. *Bull. Amer. Meteor. Soc.*, **95**, 571–583, doi:10.1175/BAMS-D-12-00172.1.

Zhang, W., and Coauthors, 2016: Improved simulation of tropical cyclone responses to ENSO in the western North Pacific in the high-resolution GFDL HiFLOR coupled climate model. *J. Climate*, **29**, 1391–1415, doi:10.1175/JCLI-D-15-0475.1.